

**NASA CONTRACTOR
REPORT**

NASA CR-2904



NASA CR-2904

0061733



**LOAN COPY: RETURN TO
AFWL TECHNICAL LIBRARY,
KIRTLAND AFB, N. M. /**

**FLUID MECHANICAL MODEL
OF THE HELMHOLTZ RESONATOR**

Alan S. Hersh and Bruce Walker

Prepared by
HERSH ACOUSTICAL ENGINEERING
Chatsworth, Calif. 91311
for Lewis Research Center



NATIONAL AERONAUTICS AND SPACE ADMINISTRATION • WASHINGTON, D. C. • SEPTEMBER 1977



0061733

1. Report No. NASA CR-2904		2. Government Accession No.		3. Recipient's Catalog No. 0061733	
4. Title and Subtitle FLUID MECHANICAL MODEL OF THE HELMHOLTZ RESONATOR				5. Report Date September 1977	
				6. Performing Organization Code	
7. Author(s) Alan S. Hersh and Bruce Walker				8. Performing Organization Report No. None	
				10. Work Unit No.	
9. Performing Organization Name and Address Hersh Acoustical Engineering 9545 Cozycroft Avenue Chatsworth, California 91311				11. Contract or Grant No. NAS3-18542	
				13. Type of Report and Period Covered Contractor Report	
12. Sponsoring Agency Name and Address National Aeronautics and Space Administration Washington, D. C. 20546				14. Sponsoring Agency Code	
15. Supplementary Notes Final report. Project Manager, Edward J. Rice, V/STOL and Noise Division, NASA Lewis Research Center, Cleveland, Ohio 44135					
16. Abstract A semi-empirical fluid mechanical model of the acoustic behavior of Helmholtz resonators is presented which predicts impedance as a function of the amplitude and frequency of the incident sound pressure field and resonator geometry. The model assumes that the particle velocity approaches the orifice in a spherical manner. The incident and cavity sound fields are connected by solving the governing oscillating mass and momentum conservation equations. The model is in agreement with the Rayleigh slug-mass model at low values of incident sound pressure level. At high values, resistance is predicted to be independent of frequency, proportional to the square root of the amplitude of the incident sound pressure field, and virtually independent of resonator geometry. Reactance is predicted to depend in a very complicated way upon resonator geometry, incident sound pressure level, and frequency. Nondimensional parameters are defined that divide resonator impedance into three categories corresponding to low, moderately low, and intense incident sound pressure amplitudes. The two-microphone method was used to measure the impedance of a variety of resonators. The data were used to refine and verify the model.					
17. Key Words (Suggested by Author(s)) Sound absorbers; Acoustics; Acoustic impedance; Nonlinear acoustic impedance			18. Distribution Statement Unclassified - unlimited STAR Category 71		
19. Security Classif. (of this report) Unclassified		20. Security Classif. (of this page) Unclassified		21. No. of Pages 73	22. Price* A04



TABLE OF CONTENTS

1.	INTRODUCTION.....	1
2.	FLUID MECHANICAL MODEL.....	3
2.1	Approach.....	4
2.2	Derivation of Governing Equations.....	4
2.3	Boundary Conditions.....	8
2.4	The Linear Regime.....	9
2.4.1	Analytic Solution for $\epsilon = 0$	11
2.4.2	Weakly Nonlinear Solution.....	15
2.5	Nonlinear Regime.....	18
3.	EXPERIMENTAL PROGRAMS.....	23
3.1	Measurement System.....	23
3.2	Linear Regime.....	24
3.2.1	The $\epsilon = 0$ Case.....	24
3.2.2	Weakly Nonlinear Case.....	26
3.3	Nonlinear Regime.....	27
4.	CONCLUSIONS.....	31
	REFERENCES.....	34
	FIGURES.....	37
	APPENDIX A - Derivation of Nonlinear Fourier Coefficients..	50
	APPENDIX B - Correction of High SPL Data For Thin Orifice Face Plates.....	60

DEFINITION OF SYMBOLS

<u>Symbol</u>	<u>Definition</u>
A	constant defined in Appendix A
A_i	Airy function
c	speed of sound
C_D	orifice discharge coefficient
d	orifice diameter
d_e	orifice inertial length defined by Eq. (24)
D	cavity diameter
E	small parameter $[\rho(\omega L_e)^2/P_i]^{1/2}$
f, \tilde{f}, g	special functions defined in text
F, G	special functions defined in text
k	acoustic wave number (ω/c)
K	constant defined by Eq. (7c)
L	cavity depth
L_e	resonator characteristic length
M	ratio of orifice maximum velocity to speed of sound (q/c)
m, n	special constants defined in Appendix A
P	sound pressure amplitude
q	maximum orifice outlet velocity
r	radial coordinate
R	resonator specific acoustic resistance
R_d	orifice diameter based Reynolds number ($\omega d^2/\nu$)
R_e	characteristic length based Reynolds number ($\omega L_e^2/\nu$)
s	small parameter defined in Appendix A
S	orifice area ($\pi d^2/4$)
SPL	sound pressure level
t	time
T	time variable defined in Appendix A
u', v', w'	radial polar and azimuthal acoustic particle velocity components
V	volume of resonator cavity
X	resonator specific acoustic reactance
$Y_0(\eta), Y_1(\eta)$	special functions defined in Appendix A
Z	resonator specific acoustic impedance

<u>Symbol</u>	<u>Definition</u>
α	resonator absorption coefficient defined by Eq. (63)
β	small parameter ($\omega L_e/c$)
ϵ	small parameter [$P_i/\rho(\omega L_e)^2$] defined by Eq. (32)
ν	fluid kinematic viscosity
μ	fluid coefficient of viscosity
ρ	fluid density
λ	sound wavelength
ω	sound radian frequency
θ	spherical polar angle
ϕ	spherical azimuthal angle
$\phi_{ci} = -\phi_{ic}$	phase angle difference between the incident and cavity sound pressures ($P_c/P_i = P_c/P_i e^{i\phi_{ic}}$)
η	transformed time coordinate defined by Eq. A-15
τ	transformed time coordinate ($\pi/2 - t$); also orifice thickness
σ	orifice to cavity area ratio $(d/D)^2$

Subscripts

e	effective
i	incident (sound field)
o	lowest order
1	first order
c	cavity
ci	refers to difference between cavity and incident sound fields
ori	refers to resonator orifice area-averaged value
res	denotes resonance
r	refers to reflected wave

Superscripts

($\dot{\quad}$)	denotes time differentiation
(\quad)'	denotes differentiation with respect to the independent variable, also denotes acoustic quantities
(\quad)*	denotes dimensional quantity

SUMMARY

A semi-empirical fluid mechanical model of the acoustic behavior of Helmholtz resonators is presented which predicts impedance as a function of the amplitude and frequency of the incident sound pressure field and resonator geometry. The model assumes that the particle velocity approaches the orifice in a spherical manner. The incident and cavity sound fields are connected by solving the governing oscillating mass and momentum conservation equations. The model is in agreement with the Rayleigh slug-mass model at low values of incident sound pressure level. At high values, resistance is predicted to be independent of frequency, proportional to the square root of the amplitude of the incident sound pressure field, and virtually independent of resonator geometry. Reactance is predicted to depend in a very complicated way upon resonator geometry, incident sound pressure level, and frequency. Nondimensional parameters are defined that divide resonator impedance into three categories corresponding to low, moderately low, and intense incident sound pressure amplitudes.

The two-microphone method was used to measure the impedance of a variety of resonators. The data were used to refine and verify the model.

1. INTRODUCTION

Helmholtz resonators are currently being used as devices to control the intense sound fields generated within jet engines. Despite its extensive application, the acoustic behavior of the Helmholtz resonator is not well understood. As part of the NASA Lewis Research Center Basic Noise Research Program, a fluid mechanical model has been derived describing the acoustic behavior of the Helmholtz resonator as a function of resonator geometry, incident sound pressure level and frequency.

Rayleigh¹ credits Helmholtz as the originator of the first theoretical analysis describing the acoustic behavior of small cavity-backed resonators - appropriately called today the Helmholtz resonator. In a recent paper, Junger² reviewed briefly the historical use of the Helmholtz resonators. Apparently, they were used by the Greeks to provide for a reverberation time in their open-air theaters. They were also used in Swedish and Danish churches as early as the thirteenth century.

Rayleigh predicted the impedance of cavity-backed orifices by using the concept of lumped elements in a simple slug-mass mechanical oscillator analogy. His model is essentially non-fluid mechanical but predicts quite accurately resonance frequency when an empirical end correction is added to the slug mass. Rayleigh's derivation is quite straight-forward. He assumed that the mass contained in an orifice of thickness τ^* and diameter d^* moves as a solid body when excited by an incident sound field. Crandall³ was one of the first to use fluid mechanical concepts to analyze the behavior of the sound fields near orifices. He solved for the friction resistance for the case of very long thin orifices (i.e., $\tau^* \gg d^*$) by assuming that the flow within the orifice is viscously fully-developed, one-dimensional, and excited by an oscillatory driving pressure gradient that is independent of the orifice axial coordinate. In a later study, Ingard⁴ modified Crandall's solution by including additional terms due to frictional losses over the wall containing the orifice. Based on both Crandall's earlier work and on further experimental and analytical studies, Ingard derived the following approximate prediction of the impedance of Helmholtz resonators exposed to weak sound waves

$$Z^* \approx \left[\underbrace{\frac{\rho^* c^* k^{*2} S^*}{2\pi}}_{\text{radiation}} + \underbrace{\rho^* \omega^* (\tau^* + d^*) \sqrt{\frac{8\nu^*}{\omega^* d^{*2}}}}_{\text{viscous}} \right] + i \left[\underbrace{\rho^* \omega^* \left(\tau^* + \frac{0.85 d^*}{1 + 0.625(d^*/\tau^*)} \right)}_{\text{inertial}} - \underbrace{\frac{\rho^* c^{*2} S^*}{V^* \omega^*}}_{\text{stiffness}} \right] \quad (1)$$

The impedance, as predicted by Eq. (1), is constant independent of the amplitude of the incident sound pressure for a specified fluid, sound frequency, and resonator geometry. Herein this will be called "linear" impedance. In 1935, Sivian⁵ observed that at high sound pressure amplitudes, the impedances of Helmholtz resonators are not constant but, instead, are strongly affected by the amplitude of the

incident sound pressure. Herein, this will be called "nonlinear" impedance. Sivian observed experimentally and confirmed theoretically that the acoustic resistance of resonators are, at sufficiently high sound pressures, linearly *proportional* to the acoustic particle velocity in the orifice. Sivian's studies prompted a variety of theoretical and experimental studies to understand and predict the behavior of Helmholtz resonators at high sound pressure levels. Mellin⁶ has recently reviewed the historical development of most of this work. In terms of predicting the nonlinear behavior of Helmholtz resonators, the work of Ingard and Ising⁷, Sirignano⁸, Zinn⁹ and Hersh and Rogers¹⁰ are particularly important.

Ingard and Ising conducted a detailed experimental investigation of the nonlinear behavior of an isolated orifice. By measuring simultaneously the amplitude and phase of the sound pressure within the cavity and the particle velocity within the orifice (using a hot wire apparatus) they concluded that for low cavity sound pressure levels, the orifice resistance and reactance were in essential agreement with that predicted by Rayleigh's slug-mass model. At high cavity sound pressure levels, the measurements showed that the orifice resistance varied *linearly* with orifice (centerline) particle velocity; the measurements also showed that the orifice reactance was very insensitive to the cavity sound pressure level decreasing at the very highest measured cavity sound pressure levels to roughly one-half its linear value. Ingard and Ising interpreted the orifice resistance data in terms of Bernouilli's Law suggesting that the flow behavior through the orifice is quasi-steady. The hot-wire measurements indicated that at these high sound pressure levels, the flow separates at the orifice forming a high velocity jet. Thus during one half cycle, the flow incident to the orifice is irrotational, but is highly rotational (in the form of jetting) after exiting from the orifice. During the other half of the cycle, the flow pattern is reversed. The loss of one-half of the reactance at these high pressure levels was accounted for by assuming that one half of the end correction is "blown" away by the exiting jet (in their experiments $\tau^*/d^* \ll 1$ hence from Eq.(1) most of the reactance is due to the end correction). Ingard and Ising also measured the particle velocity as a function of axial distance from the orifice. They found that the inflow velocity rapidly decayed to very small values at distances of about two to three diameters from the orifice.

Initially Sirignano and later Zinn, recognizing that Rayleigh's slug-mass model was incapable of accounting for the jetting of fluid from the orifice, used fluid mechanical concepts to predict the behavior of the Helmholtz resonator. To simplify their models, they assumed that the characteristic dimensions of both the orifice and cavity are very much smaller than the incident acoustic wavelength and, further, that the acoustic flow through the orifice is one-dimensional, incompressible, quasi-steady, and calorically perfect.

Both authors base their models on an integral formulation of the conservation of mass and momentum applied to two control volumes, one being the volume bounded by the orifice inlet and outlet surfaces

and the other the cavity. To solve these integrals, they used the method of successive approximations with the first order solution corresponding to the linear case of very small sound pressures incident to an orifice. The orifice nonlinear behavior is introduced through the higher order terms and represents only a second order approximation to the (linear) first order solution. Thus their conclusions apply only to weakly nonlinear acoustic pressures and not to the intense sound pressures existing within rocket chambers or jet engines, the intended application of their models.

Hersh and Rogers assumed that the acoustic inflow in the immediate vicinity of an orifice can be modelled as a locally spherical flow. Near the orifice, the particle flow is to a first approximation, unsteady and incompressible-referred to as the near field. An analytical model was presented of the behavior of orifices exposed to intense sound pressure fields which showed that orifice impedance to be dominated by particle flow nonlinearity. This model establishes explicitly the quasi-steady behavior of orifices exposed to intense sound fields.

The approach used by Hersh and Rogers is applied in Section 2 below to derive a semi-empirical fluid mechanical model of the nonlinear acoustic behavior of Helmholtz resonators. In Section 3, experimental data, obtained using the two-microphone method to measure resonator impedance, is used to both support and verify the model. The principal findings of the study are summarized in Section 4.

2. FLUID MECHANICAL MODEL

A fluid mechanical model of the behavior of Helmholtz resonators is described below. The model has been idealized sufficient to permit mathematical solution without compromising important physical characteristics. The derivation is divided into two categories, one corresponding to weak or moderately weak incident sound fields and the other to very intense incident sound fields.

The model is based on the following key assumptions:

(1) Sound waves approach the neighborhood of the resonator orifice in a spherical manner. The three-dimensionality of the sound field will account for the large changes in acoustic particle velocity measured by Ingard and Ising. For this assumption to be valid the orifice diameter must be very small relative to the incident sound wavelength (i.e., $d^* \ll \lambda^*$ - orifice geometry is defined in Fig. 1).

(2) The acoustic pressure and density are adiabatically related. Further, the incident sound is simple harmonic.

(3) The amplitude of the incident acoustic pressure is small compared to the ambient pressure.

2.1 Approach

Consider the special case of a sound wave approaching a resonator with its wavenumber k perpendicular to the plane surface containing the orifice (i.e., the cross-hatched surface shown in Fig. 2a). From this and assumption (1) above, the incident sound particle velocity field near the orifice is modelled as spherical and independent of the azimuthal angle ϕ . A sketch of the flow is shown entering the resonator cavity in Fig. 2b. The principal advantage of the model is its simplification of the governing equations of motion. Its principal disadvantage is its inability to accurately model the particle velocity entering the resonator cavity. This is illustrated in Fig. 2b wherein the spherical inflow model is singular at the virtual origin $r^*=0$; deviations from a truly spherical flow are required in order to permit the flow to enter the orifice in an axial manner. To avoid this singularity, the (spherical) flow field is truncated at a hemispherical surface $r^*=L_e^*$ defined such that at this surface the particle volume flow rate is equal to the actual particle volume flow rate entering the cavity. The consequence of this limitation is that the characteristic surface radius L_e^* must be determined experimentally. This is discussed in more detail later.

The spherical inflow model described above is assumed to be valid only during the half-cycles corresponding to particle inflow. The hot-wire measurements conducted by Ingard and Ising showed that at moderate and higher sound pressure amplitudes the outflow particle velocity field separated within the orifice forming a highly rotational jet. They further observed the particle flow to be symmetrical with respect to inflow and outflow. Thus a solution valid during the inflow half-cycle should via conservation of particle mass into and out of the cavity be valid throughout the cycle.

The background material described above provides the basis for the following approach. First continuity and momentum conservation equations governing the motion of a harmonically driven spherically symmetric particle inflow are derived. Second, the resulting equations of motion are normalized by appropriately scaling the dependent and independent variables. The resulting equations are then simplified by retaining only the important terms. Separate equations of motion are then derived for the "linear" case (constant or almost constant impedance) and the "nonlinear" case (variable impedance). Third, the equations of motion are solved so as to satisfy two boundary conditions imposed by the pressure field. One is that the near field pressure must merge smoothly (asymptotically) into the harmonically oscillating incident pressure. The other is that at the hemispherical surface $r^*=L_e^*$ (see Fig. 2b), the near field pressure must be equal to the instantaneous cavity pressure.

2.2 Derivation of Governing Equations

The flow field is assumed to consist of a steady-state part containing no flow and an oscillating part. Assuming spherically symmetric inflow, the conservation of oscillating mass and momentum

may be written approximately

$$r^{*2} \frac{\partial p^{*1}}{\partial t^*} + \rho^* \frac{\partial}{\partial r^*} (r^{*2} u^{*1}) + r^{*2} u^{*1} \frac{\partial \rho^{*1}}{\partial r^*} = 0 \quad (2a)$$

$$\frac{\partial u^{*1}}{\partial t^*} + u^{*1} \frac{\partial u^{*1}}{\partial r^*} + \frac{1}{\rho^*} \left(1 - \frac{\rho^{*1}}{\rho^*}\right) \frac{\partial p^{*1}}{\partial r^*} - v^* \left[\frac{1}{r^{*2}} \frac{\partial}{\partial r^*} (r^{*2} \frac{\partial u^{*1}}{\partial r^*}) - 2 \frac{u^{*1}}{r^{*2}} + \frac{1}{r^{*2} \sin \theta} \frac{\partial}{\partial \theta} (\sin \theta \frac{\partial u^{*1}}{\partial \theta}) \right] = 0 \quad (2b)$$

$$\left(1 - \frac{\rho^{*1}}{\rho^*}\right) \frac{\partial p^{*1}}{\partial \theta} - \frac{2\mu^*}{r^*} \frac{\partial u^{*1}}{\partial \theta} = 0 \quad (2c)$$

where ()' denotes fluctuating terms.

Equation (2c) shows that the pressure gradient in the θ direction is proportional to μ^* which is quite small for most fluids of interest (viz. air). Hence the momentum balance in the θ direction will be ignored.

Equations (2a,b) can be simplified by proper normalization of the various terms and retaining only those of importance. The idea here is to try to anticipate the order-of-magnitude of the changes of the various terms in order to rank order their relative importance. To start with, the amplitude of the incident sound field P_i^* is assumed to characterize the acoustic pressure change external to the resonator orifice, P_i^*/c^{*2} the density change (recall that the acoustic pressure and density are adiabatically related), q^* the particle velocity change, L_e^* the length scale and ω^{*-1} the time scale.

The selection of the magnitude of the various normalization quantities above requires special comment. The hemispherical radius L_e^* is chosen to characterize the scale of the displacement of the sound particle field near the orifice. Because of the spherical inflow assumption, the behavior of the particle displacement L_e^* will be determined indirectly from measurements described in Section 3. The time scale ω^{*-1} is obvious as the response of the cavity is driven by the harmonic incident sound field. The selection of P_i^* and q^* is based on the experimental findings of Ingard and Ising. Their experimental data showed that two distinct regimes exist depending upon the amplitude P_i^* of the incident sound field. For sufficiently low values of P_i^* (the "linear" regime wherein orifice inertial reactance is much larger than orifice resistance),

$$P_i^* = \rho^* \omega^* L_e^* q^* ; \quad \frac{q^*}{\omega^* L_e^*} = \frac{P_i^*}{\rho^* (\omega^* L_e^*)^2} \ll 1 \quad (3a)$$

and for sufficiently high values of P_i^* (the "nonlinear" regime wherein orifice resistance is much larger than orifice inertial reactance),

$$P_i^* = \rho^* q^{*2} ; \quad \frac{\omega^* L_e^*}{q^*} = \sqrt{\frac{\rho^* (\omega^* L_e^*)^2}{P_i^*}} \ll 1 \quad (3b)$$

Introducing the nondimensional variables r, t, u, p, ρ defined as

$$r^* = L_e^* r ; \quad t^* = \omega^{*-1} t ; \quad u^* = q^* u ; \quad p^* = P_i^* p ; \quad \rho^* = \frac{P_i^*}{c^{*2}} \rho, \quad (4)$$

the continuity and momentum equations may be written

$$\left(\frac{P_i^*}{\rho^* c^{*2}} \right) \left(\frac{\omega^* L_e^*}{q^*} \right) (r)^2 \frac{\partial p}{\partial t} + \frac{\partial}{\partial r} (r^2 u) + \left(\frac{P_i^*}{\rho^* c^{*2}} \right) (r)^2 u \frac{\partial p}{\partial r} = 0 \quad (5a)$$

$$\begin{aligned} \frac{\partial u}{\partial t} + \left(\frac{q^*}{\omega^* L_e^*} \right) u \frac{\partial u}{\partial r} + \left(\frac{P_i^*}{\rho^* \omega^* L_e^* q^*} \right) \left[1 - \left(\frac{P_i^*}{\rho^* c^{*2}} \right) p \right] \frac{\partial p}{\partial r} \\ - \frac{v^*}{\omega^* L_e^{*2}} \left[\frac{1}{(r)^2} \frac{\partial}{\partial r} \left((r)^2 \frac{\partial u}{\partial r} \right) - \frac{2u}{(r)^2} + \frac{1}{(r)^2 \sin^2 \theta} \frac{\partial}{\partial \theta} \left(\sin \theta \frac{\partial u}{\partial \theta} \right) \right] = 0 \end{aligned} \quad (5b)$$

The importance of the various terms in Eqs. (5a,b) are determined solely by the magnitude of their coefficients (recall that the dimensionless terms have been normalized to be of order unity). To rank order them, the governing equations are divided into the linear regime where Eqs. (3a) apply and the nonlinear regime where Eqs. (3b) apply.

Consider first the linear regime. The small parameters ϵ and β are introduced where

$$\epsilon = \frac{P_i^*}{\rho^* (\omega^* L_e^*)^2} \ll 1 ; \quad \beta = \frac{\omega^* L_e^*}{c^*} \ll 1 \quad (6)$$

Assuming that L_e^* is of the order of d^* , then $\beta \ll 1$ for most aircraft applications. β is shown below to be a measure of the importance of fluid compressibility. Substituting these parameters into the continuity and momentum equations, the behavior of weak sound waves approaching the resonator orifice may be written

$$\beta^2 r^2 \frac{\partial p}{\partial t} + \frac{\partial}{\partial r} (r^2 u) + \epsilon \beta^2 r^2 u \frac{\partial p}{\partial r} = 0 \quad (7a)$$

$$\frac{\partial u}{\partial t} + \epsilon u \frac{\partial u}{\partial r} + (1 - \epsilon \beta^2 p) \frac{\partial p}{\partial r} \left(\frac{\gamma^*}{\omega^* L_e^*} \right) \left(\begin{array}{c} \text{viscous} \\ \text{terms} \end{array} \right) = 0 \quad (7b)$$

An examination of the various terms in Eq. (7a) the continuity equation, shows that: 1) the second term, which represents the divergence of the volume velocity, is of order unity and is by far the most important term; 2) the first term, which is a measure of the fluid compressibility, is very much smaller than the second term and 3) the third term, which takes into account the fluid nonlinearity, is the the smallest. Thus the flow field for the case of weak sound waves approaching the resonator orifice behaves predominately as unsteady and incompressible. This incompressible behavior of the flow field near the resonator orifice is consistent with the large changes in acoustic velocity measured by Ingard and Ising. Since the changes occurred over a distance very much smaller than the sound wavelength, they represent hydrodynamic rather than acoustic changes.

For the nonlinear regime, it is convenient to introduce the small parameters M and E defined as

$$M^2 = \left(\frac{q^*}{c^*} \right)^2 = \frac{P_i^*}{\rho^* c^{*2}} \ll 1; \quad E = \sqrt{\frac{\rho^* (\omega^* L_e^*)^2}{P_i^*}} \ll 1 \quad (8)$$

The restriction that $M^2 \ll 1$ follows from assumption (3) and Eq. (3b) above. The restriction that $E \ll 1$ follows from the assumption that the amplitude of the incident sound pressure field is large. Substituting the parameters into the continuity and momentum equations yield

$$M^2 E \frac{\partial p}{\partial t} + \frac{\partial}{\partial r} (r^2 u) + M^2 r^2 u \frac{\partial p}{\partial r} = 0 \quad (9a)$$

$$E \frac{\partial u}{\partial t} + u \frac{\partial u}{\partial r} + (1 - M^2 p) \frac{\partial p}{\partial r} - \left(\frac{\gamma^*}{q^* L_e^*} \right) \left(\begin{array}{c} \text{viscous} \\ \text{terms} \end{array} \right) = 0 \quad (9b)$$

Consistent with the linear regime, the continuity equation governing the nonlinear regime also behaves as if the sound field is unsteady and incompressible. Equation (9a) differs from Eq. (7a) in one interesting aspect. The third term in Eq. (9a) which is a measure of the importance of nonlinearity is larger by the amount $1/E$ than the first term which is a measure of the importance of compressibility. The converse is true for the linear case. Thus, the normalization for

the two regimes reveals an ordering among the various terms that is consistent and, therefore, lend credence to the validity of the approach.

2.3 Boundary Conditions

The governing equations of motion must satisfy two boundary conditions both of which are imposed upon the fluctuating pressure field during the half cycles corresponding to particle flow into the cavity. The boundary conditions provide the connection missing in previous studies between the instantaneous pressure within the resonator cavity and the harmonically oscillating driving pressure incident to the resonator orifice. One of the boundary conditions requires the near field pressure to merge smoothly (asymptotically) into the incident pressure. In dimensional terms, this boundary condition is written as

$$\text{Limit}_{r \rightarrow \infty} p^*(r, t^*) = P_i^* \cos(\omega^* t^*) \quad (10a)$$

In nondimensional terms, Eq. (10a) becomes

$$\text{Limit}_{r \rightarrow \infty} p(r, t) = \cos(t) \quad (10b)$$

Using the Ingard and Ising hot-wire measurements as a guide, $r^* = \infty$ corresponds practically to a radial distance of about three orifice diameters. Thus, when $r^* > 3d^*$ the oscillating pressure field will be assumed to be outside the near field influence of the orifice.

The other boundary condition is considerably more complicated principally because of difficulties associated with the spherical inflow model. This boundary condition requires the fluctuating near field pressure at the hemispherical surface $r^* = L_e^*$ (recall that at this surface the particle volume flow rate $2\pi L_e^{*2} q^*$ is equal to the actual volume flow rate entering the resonator cavity) to be equal to the instantaneous cavity pressure. The connection between the time pressure history of the cavity pressure and the particle flow rate into the cavity follows immediately from the adiabatic relationship between the cavity pressure and density written in dimensional terms,

$$\frac{\partial p_c^*}{\partial t^*} = c^{*2} \frac{\partial \rho_c^*}{\partial t^*} = - \frac{c^{*2} \rho^* 2\pi L_e^{*2} q^*(r^* = L_e^*, t^*)}{V^*} \quad (11a)$$

where $2\pi L_e^{*2} q^*(r^* = L_e^*, t^*)$ is the instantaneous volume velocity flow rate entering the cavity volume V^* . The negative sign is used because q^* is negative for inward directed spherical flow (see Fig. 2b). Using Eq. (4) to nondimensionalize Eq. (11a) yields

$$\frac{\partial p_c}{\partial t} = - \left[\frac{2\pi L_e^{*2} \rho^* c^{*2} q^*}{\omega^* V^* P_i^*} \right] u(r = 1, t) \quad (11b)$$

There are separate boundary conditions for the linear and nonlinear regimes depending upon the relationships between P_i^* and q^* given by Eqs. (3a) and (3b). For the linear regime, the nondimensionalized boundary condition is

$$\frac{\partial}{\partial t} p_c (r=1, t) = - \left[\frac{2\pi L_e^* c^{*2}}{\omega^{*2} V^*} \right] u (r=1, t) \quad (12)$$

For the nonlinear regime, the nondimensionalized boundary condition is

$$\frac{\partial}{\partial t} p_c (r=1, t) = - \left[\frac{2\pi L_e^{*2} c^{*2}}{\omega^* V^* q^*} \right] u (r=1, t) \quad (13a)$$

Equation (13a) can be rewritten in a more convenient form - this will be clear later-by replacing q^* by $\sqrt{P_i^*/\rho^*}$ from Eq. (3b) and using Eq. (8) to yield

$$\frac{\partial}{\partial t} p_c (r=1, t) = -E \left(\frac{2\pi L_e^* c^{*2}}{V^* \omega^{*2}} \right) u (r=1, t) \quad (13b)$$

There is one limitation to the derivation of the cavity pressure boundary conditions described by Eqs. (12) and (13) that must be discussed. Recall that in their derivation, the cavity pressure responds both adiabatically and instantaneously (i.e., hydrodynamically) to the particle *volume flow rate* entering the cavity. This means that the cavity pressure cannot distinguish different spatial distributions of entering particle flow (e.g. spherical or axial). For application to the proposed spherical inflow model, angular effects in the θ direction associated with boundary layers over the side walls and orifice (see Fig. 2b) will have to be accounted for *before* application of Eqs. (12) and (13). This will be discussed in more detail in Sections 2.4 and 2.5.

2.4 The Linear Regime

The solution to Eqs. (7a) and (7b) subject to the boundary conditions specified by Eqs. (10b) and (12) describe the behavior of Helmholtz resonators exposed to weak or moderately weak sound fields. In the derivation that follows, the effects of frictional losses due to the viscosity of the flow near and within the orifice are assumed to be inversely proportional to the square root of $Re (= \omega L_e^{*2} / \nu^*)$, a characteristic length based Reynolds number). This assumption is based on the recent study of the acoustic behavior of orifices by Hersh and Rogers, which showed that the retarding action of the fluid viscosity acts, for a given driving excitation pressure, to decrease the magnitude of the acoustic velocity pumped through an orifice by an amount proportional to the local boundary layer displacement thickness along the orifice side walls. This is equivalent to assuming that the oscillating

boundary layer flow is laminar. Adoption of these assumptions will result in a particle inflow that is compatible with the cavity pressure response boundary condition defined by Eq. (12). Recall that in the derivation of these boundary conditions, the spherical particle inflow was assumed to be independent of the angle θ . Incorporating the above, Eq. (7b) may be rewritten

$$\frac{\partial u}{\partial t} + \varepsilon u \frac{\partial u}{\partial r} + (1 - \varepsilon \beta^2 p) \frac{\partial p}{\partial r} + \frac{K}{\sqrt{Re}} u = 0 \quad (7c)$$

Here K is a constant that will be evaluated experimentally. Equations (7a) and (7c) are further simplified by retaining terms to order ε (since $\beta \ll 1$, the effects of compressibility would only weakly affect resonator behavior-hence are ignored) to yield

$$\frac{\partial}{\partial r} (r^2 u) = 0 \quad (14a)$$

$$\frac{\partial u}{\partial t} + \varepsilon u \frac{\partial u}{\partial r} + \frac{\partial p}{\partial r} + \frac{K}{\sqrt{Re}} u = 0 \quad (14b)$$

Integrating Eq. (14a) with respect to r yields

$$u(r, t) = -F(t; \varepsilon; Re)/r^2 \quad (15)$$

where $F(t; \varepsilon; Re)$ is an arbitrary function of integration. The negative sign again denotes that the particle velocity is directed inwards towards the resonator orifice. Substituting Eq. (15) into the radial momentum equation (Eq. 14b) yields

$$\frac{\partial}{\partial r} \left(\dot{F} + \frac{\varepsilon F^2}{2r^4} + p + \frac{K}{\sqrt{Re}} \frac{F}{r} \right) = 0 \quad (16)$$

The ($\dot{}$) notation denotes differentiation with respect to time. Integrating with respect to r yields

$$\frac{\dot{F}}{r} + \frac{\varepsilon F^2}{2r^4} + p + \frac{K}{\sqrt{Re}} \frac{F}{r} = T(t) \quad (17)$$

where $T(t)$ is another arbitrary function of integration. From application of the boundary condition given by Eq. (10b), $T(t) = \cos(t)$. The boundary

condition given by Eq. (12) relates the instantaneous cavity pressure $P_c(t; Re)$ to the instantaneous particle velocity $u(r=1, t)$ entering the orifice at $r=1$ (recall again that to avoid the singularity at $r=0$ associated with the spherical inflow assumption, the flow was arbitrarily truncated at the hemispherical surface $r=1$). To incorporate this boundary condition, Eq. (17) is differentiated with respect to time, r is set equal to unity ($r=1$) and Eq. (12) and $T(t)=\cos(t)$ substituted to yield

$$\ddot{F} + \left(\frac{K}{\sqrt{Re}} + \epsilon F \right) \dot{F} + \left(\frac{c^{*2} 2\pi L_e^*}{V^* \omega^{*2}} \right) F = -\sin(t) \quad (18)$$

Equation (18) in its present form is misleading. It is valid only during the half-cycles associated with particle inflow. To properly model the particle velocity throughout all cycles Eq. (18) should be written

$$\ddot{F} + \left(\frac{K}{\sqrt{Re}} + \epsilon |F| \right) \dot{F} + \left(\frac{c^{*2} 2\pi L_e^*}{V^* \omega^{*2}} \right) F = -\sin(t) \quad (18a)$$

The motivation here is that during each half cycle the coordinate system must be switched to the appropriate side of the resonator orifice corresponding to particle inflow. While the linear terms account for this automatically the nonlinear term, ϵFF does not. An alternate explanation is that the *coefficient of F represents the system damping which must always be positive.*

The solution to Eq. (18a) yields directly, upon combining it with Eq. (15), the time and space behavior of the acoustic particle velocity field incident to the resonator. Because of its complexity, only an approximate solution will be sought. An analytic solution is possible, however, for the special case $\epsilon = 0$.

2.4.1 Analytic Solution for $\epsilon = 0$

Setting $\epsilon = 0$, Eq. (18a) reduces to the linear equation

$$\ddot{F} + \frac{K}{\sqrt{Re}} \dot{F} + \left(\frac{c^{*2} 2\pi L_e^*}{V^* \omega^{*2}} \right) F = -\sin(t) \quad (19)$$

Only the particular solution is of interest because the homogeneous solutions exhibit a time decay proportional to $\exp[-Kt/2\sqrt{Re}]$, hence do not contribute to the steady-state behavior. The solution to the above equation, written in complex notation where it is understood that only the real part has physical meaning, is

$$F(t) = \frac{e^{it}}{\frac{K}{\sqrt{Re}} + i \left(1 - \frac{2\pi L_e^* c^{*2}}{V^* \omega^{*2}} \right)} \quad (20)$$

The particle velocity follows immediately by substituting $F(t)$ above into Eq. (15)

$$u(r, t; Re) = \frac{-e^{it}}{r^2 \left[\frac{K}{\sqrt{Re}} + i \left(1 - \frac{2\pi L_e^* c^{*2}}{V^* \omega^{*2}} \right) \right]} \quad (21)$$

The impedance of Helmholtz resonators is often defined in the literature as the (complex) ratio of the incident driving acoustic pressure ($P_i = e^{it}$) to the "orifice area-averaged" particle velocity (u_{ori}). To use this definition, it will be necessary to relate the particle velocity at the reference hemispherical surface of area ($2\pi L_e^{*2}$) to another hemispherical surface whose area is equal to the orifice area ($\pi d^{*2}/4$). Using Eq. (15) which represents the conservation of particle mass for spherical inflow, the orifice area averaged particle inflow is

$$u_{ori} = \left[\frac{2\pi L_e^{*2}}{\frac{\pi d^{*2}}{4}} \right] u(r=1, t; Re) = -8 \left(\frac{L_e^*}{d^*} \right)^2 e^{it} / \left[\frac{K}{\sqrt{Re}} + i \left(1 - \frac{2\pi L_e^* c^{*2}}{V^* \omega^{*2}} \right) \right]$$

The impedance of the Helmholtz resonator follows immediately to be

$$(-Z)_{ori} = \frac{p(r=\infty, t)}{u_{ori}} \approx \frac{1}{8} \left(\frac{d^*}{L_e^*} \right)^2 \frac{K}{\sqrt{Re}} + i \frac{1}{8} \left(\frac{d^*}{L_e^*} \right)^2 \left[1 - \frac{2\pi L_e^* c^{*2}}{V^* \omega^{*2}} \right] \quad (22)$$

From Eq. (22), resonance is defined to occur at zero reactance. This occurs at a radian frequency given by

$$\omega^{*2} = \omega_{res}^{*2} = \frac{2\pi L_e^* c^{*2}}{V^*} \quad (23)$$

Equation (22) provides for a rigorous definition of the characteristic length L_e^* . Setting the reactance specified in Eq. (1) equal to zero yields the following well known expression for the resonance frequency of Helmholtz resonators,

$$\omega_{res}^{*2} = \frac{\pi d^{*2}}{4} \frac{c^{*2}}{V^* d_e^*} \quad (23a)$$

where

$$d_e^* = \tau_+^* \frac{0.85 d^*}{1 + 0.625 \left(\frac{d^*}{D^*}\right)} \quad (24)$$

is interpreted as the orifice "effective" inertia length. Combining Eq. (23a) and Eq. (22) and solving for the characteristic length L_e^* leads to its definition

$$L_e^* = \frac{V^* \omega^{*2} r_{es}^2}{2\pi c^{*2}} = \frac{1}{8} \left(\frac{d^*{}^2}{d_e^*}\right) \quad (25)$$

Thus the characteristic length L_e^* is independent of the cavity volume V^* or the details of the incident sound pressure level and frequency - it is dependent primarily upon the orifice thickness and diameter.

Equation (25) can be used to define an orifice discharge coefficient (C_D) characteristic of Helmholtz resonators operating in the "linear" regime. The discharge coefficient is defined as the ratio of the orifice area-averaged particle velocity to the maximum particle velocity entering the cavity. This definition is equivalent to that used to define the discharge coefficient of orifices exposed to steady-state flow. Since the maximum particle inflow occurs at the hemispherical surface ($r=1$), the discharge coefficient is easily computed to be,

$$C_D \equiv \frac{u_{ori}}{u_{max}} = \frac{2\pi L_e^{*2}}{\frac{\pi d^{*2}}{4}} = \frac{1}{8} \left(\frac{d^*{}^2}{d_e^*}\right)^2 \quad (26)$$

Since $d_e^* \approx d^*$ for most orifice geometries of practical interest to the aircraft industry, C_D is a small number. Mellin's review paper shows that low values of steady state discharge coefficients occur whenever the flow through the orifice is viscously controlled. This is certainly consistent with the above derivation which shows the orifice resistance to be controlled by laminar boundary-layer losses.

With L_e^* defined by Eq. (25), the final form of the nondimensionalized resonator impedance is

$$(-Z)_{ori} = 8 \left(\frac{d_e^*}{d^*}\right)^2 \frac{K}{\sqrt{Re}} + i \left(1 - \frac{c^{*2} S^*}{V^* \omega^{*2} d_e^*}\right) \quad (27a)$$

In *dimensional* terms, the resonator impedance is

$$(-Z)_{ori}^* = 8K \left(\frac{d_e^*}{d^*}\right)^2 \sqrt{\rho^* \mu^* \omega^*} + i \left(\rho^* \omega^* d_e^* - \frac{\rho^* c^{*2} S^*}{V^* \omega^*}\right) \quad (27b)$$

where $S^* = \pi d^{*2}/4$ is the orifice cross-sectional area. Equation (27b) compares favorably with Eq. (1), the slug-mass model providing the constant K is appropriately defined and the radiation resistance term in Eq. (1) is negligible.

The amplitude and phase difference between the incident and cavity sound fields are derived by combining Eqs. (12) and (21) and evaluating them at $r=1$. Using complex notation where again only the real part has physical meaning and noting that $\partial/\partial t = i$, then the instantaneous cavity pressure P_c is

$$\frac{\partial p}{\partial t}(1, t) = i p_c = e^{it} \left\{ \frac{\left(\frac{\omega_{res}^*}{\omega^*}\right)^2 \frac{K}{\sqrt{R_e}} - i \left(\frac{\omega_{res}^*}{\omega^*}\right)^2 \left[1 - \left(\frac{\omega_{res}^*}{\omega^*}\right)^2\right]}{\frac{K}{R_e} + \left[1 - \left(\frac{\omega_{res}^*}{\omega^*}\right)^2\right]^2} \right\}$$

Recalling that the nondimensionalized incident sound field $P_i = e^{it}$, then the amplitude and phase differences between the incident and cavity sound fields are

$$\left| \frac{P_c^*}{P_i^*} \right| = \frac{\left(\frac{\omega_{res}^*}{\omega^*}\right)^2}{\sqrt{\frac{K^2}{R_e} + \left[1 - \left(\frac{\omega_{res}^*}{\omega^*}\right)^2\right]^2}} \quad (28a)$$

and

$$\phi_{ic} = -\phi_{ci} = -\tan^{-1} \left\{ \frac{\frac{K}{\sqrt{R_e}}}{\left[1 - \left(\frac{\omega_{res}^*}{\omega^*}\right)^2\right]} \right\} \quad (28b)$$

At resonance, the amplitude and phase angle differences between the cavity and incident sound fields simplify to

$$\left| \frac{P_c^*}{P_i^*} \right| = \frac{\sqrt{R_e}}{K} \quad \text{and} \quad \phi_{ci} = 90 \text{ degrees} \quad (28c)$$

Thus at resonance, the amplitude difference between the cavity and incident sound field is due primarily to viscous boundary layer losses retarding the fluid motion near and within the orifice.

To summarize, the classical Helmholtz resonator impedance derived originally by assuming that the particle mass within and near the orifice moves as a solid body (i.e., the lumped mass model) upon excitation by an incident sound field has been rederived from fluid mechanical conservation laws. This has accomplished two important objectives.

First, it establishes the validity of the spherical inflow model and second, it provides a logical model to understand the nonlinear acoustic behavior of the Helmholtz resonator.

2.4.2 Weakly Nonlinear Solution

The effects of moderate increases in incident sound pressure levels are modelled by Eq. (18a). An approximate solution is sought in terms of a regular perturbation expansion in powers of ϵ , the first two terms of which are

$$F(t; R_e; \epsilon) \approx F_0(t; R_e) + \epsilon F_1(t; R_e) + \dots O(\epsilon^2)$$

Collecting coefficients of the various powers of ϵ , the leading term ($\epsilon^0=1$) is identical to Eq. (19) while the terms proportional to ϵ are

$$\ddot{F}_1 + \frac{K}{\sqrt{R_e}} \dot{F}_1 + \left(\frac{\omega_{res}^*}{\omega^*}\right)^2 F_1 = -F_0 |\dot{F}_0| \quad (29)$$

where ω_{res}^* is defined by Eq. (23).

For this approach to be valid, $|\epsilon F_1(t; R_e)| \ll |F_0(t; R_e)|$. This means that only modest deviations from the "linear" solutions described in Section 2.4.1 above are sought. This will place upper bound restrictions on the magnitude of the amplitude of the incident sound field. Nonlinear solutions only for the special case $\omega^* = \omega_{res}^*$ corresponding to resonance will be sought. This will simplify considerably the mathematical details and will provide insight regarding the effects of nonlinearity for the most important application of the Helmholtz resonator, at resonance. Substituting the real part of Eq. (20) for $F_0(t)$ into the RHS of Eq. (29) yields the following solution for the special case of $\omega^* = \omega_{res}^*$,

$$F_1(t; R_e) = \mp \frac{\sin(2t)}{\frac{6K^2}{R_e} \left[1 + \frac{4K^2}{9R_e}\right]} \mp \frac{\cos(2t)}{\frac{9K}{\sqrt{R_e}} \left[1 + \frac{4K^2}{9R_e}\right]} \quad (30)$$

where the (-) sign is valid for those half-cycles corresponding to particle inflow and the (+) sign for the particle outflow.

To predict resonator impedance, the first harmonic or fundamental component of Eq. (30) is required. Using standard Fourier analysis, it is straight-forward to show that the fundamental components are, approximately, given by

$$F_1(t; R_e) \approx -\frac{2\cos(t)}{\frac{27\pi K}{\sqrt{R_e}}} - \frac{4\sin(t)}{\frac{9\pi K}{\sqrt{R_e}}} \quad (30a)$$

Combining zeroth and first-order terms, written in complex notation where it is understood that only the real part has physical meaning, yields

$$F(t) \approx \frac{e^{it} \sqrt{R_e}}{K} \left[1 - \varepsilon \left(\frac{2}{27\pi} - i \frac{4\sqrt{R_e}}{9\pi K} \right) \right] \quad (31)$$

For Eq. (31) to be valid, the constraint that $|\varepsilon F_1(t)| < |F_0(t)|$ translates into the following constraint on ε ,

$$\left| \varepsilon \left[\frac{2}{27\pi} - i \frac{4\sqrt{R_e}}{K} \right] \right| \approx \frac{4\varepsilon \sqrt{R_e}}{K} < 1 \longrightarrow \varepsilon < \frac{K}{4\sqrt{R_e}}$$

This constraint on ε can be translated directly into the following constraint placed on the upper bound of the amplitude of the incident sound field

$$\frac{P_i^*}{\rho^*(\omega^* d^*)^2} < \frac{K}{32} \sqrt{\frac{\nu^*}{\omega^* d^*}}$$

where, from Eqs. (6) and (25)

$$\varepsilon = 64 \left(\frac{d_e^*}{d^*} \right)^2 \frac{P_i^*}{\rho^*(\omega^* d^*)^2} \quad (32)$$

Following the same procedures used in deriving the linear resonator impedance defined by Eq. (27a), the resonator orifice-area averaged impedance is, to order ε ,

$$(-Z)_{ori} \approx 8 \left(\frac{d_e^*}{d^*} \right)^2 \frac{K}{\sqrt{R_e}} \left(1 + \frac{2}{27\pi} \varepsilon \right) - i \frac{32}{9\pi} \varepsilon \left(\frac{d_e^*}{d^*} \right)^2 \quad (33a)$$

Expressed in dimensional terms,

$$(-Z)_{ori} \approx 8 \left(\frac{d_e^*}{d^*} \right)^2 K \sqrt{\rho^* \mu^* \omega^*} \left(1 + \frac{2}{27\pi} \varepsilon \right) - i \frac{4\varepsilon}{9\pi} \rho^* \omega^* d_e^* \quad (33b)$$

It is clear from Eq. (33) that the effects of moderately weak non-linearity are to increase only very slightly the resonator resistance and to decrease slightly the reactance. Following the same procedures

used to derive Eqs. (28a,b,c), the amplitude and phase differences between the cavity and incident sound fields are

$$\left| \frac{P_c^*}{P_i^*} \right| \approx \sqrt{\frac{Re}{K^2} \left(1 - \frac{4\epsilon}{27\pi} \right)} \quad (34a)$$

and

$$\phi_{ci} \approx \tan^{-1} \left[\frac{9\pi K}{4\epsilon \sqrt{Re}} \right] \quad (34b)$$

From Eqs. (34a) and (34b) it is clear that both the ratio of sound pressure amplitude and phase angle differences between the cavity and incident sound fields *decrease* with *increasing sound pressure levels*.

The decrease of reactance predicted by Eq. (33) is in agreement with that measured by Ingard and Ising. Ingard and Ising believed that the decrease was caused by a reduction of effective orifice particle inertia length (d_e^*) related to particle flow jetting from the orifice. The derivation shown below supports this interpretation. Combining the reactance terms of Eqs. (27b) and (33b) yields, in dimensional terms,

$$(-X^*)_{res} \approx \rho^* \omega^* d_e^* - \frac{\rho^* c^{*2} S^*}{V^* \omega^*_{res}} \approx -\frac{4\epsilon}{9\pi} \rho^* \omega^* d_e^* \quad (35)$$

Now assume that the effective orifice particle inertial length can be expanded as a power series in ϵ so that to order ϵ ,

$$d_e^* \approx (d_e^*)_0 + \epsilon (d_e^*)_1 \quad (36)$$

Substituting Eq. (36) for d_e^* into Eq. (35) yields, to order ϵ ,

$$\rho^* \omega^*_{res} (d_e^*)_0 + \epsilon \rho^* \omega^*_{res} (d_e^*)_1 - \frac{\rho^* c^{*2} S^*}{V^* \omega^*_{res}} = -\frac{4\epsilon}{9\pi} \rho^* \omega^* (d_e^*)_0$$

The solution for $(d_e^*)_1$, where $\rho^* \omega^*_{res} (d_e^*)_0 = \rho^* c^{*2} S^* / V^* \omega^*_{res}{}^2$, is

$$(d_e^*)_1 \approx -\frac{4\epsilon}{9\pi} (d_e^*)_0 \longrightarrow (d_e^*) \approx (d_e^*)_0 \left[1 - \frac{4\epsilon}{9\pi} \right] \quad (36a)$$

Thus, the effective orifice inertial length (d_e^*) is shown to decrease with increasing incident sound pressure level in accord with the

measurements of Ingard and Ising. The reduction of (d_e^*) suggests that flow nonlinearity transfers stored inertial energy into dissipated kinetic energy - it apparently does not affect stored (cavity) potential energy.

2.5 Nonlinear Regime

Equations (9a) and (9b) govern the behavior of Helmholtz resonators exposed to intense sound fields. In this regime, the characteristic Reynolds number $Re = \bar{q}L_e^*/v^*$ is independent of frequency in contrast to the Reynolds number $Re = \bar{\omega}L_e^{*2}/v^*$ characterizing the linear regime. Since the Reynolds number is fairly large in the nonlinear regime (Ingard and Ising measured particle speeds as high as 50 m/sec), the contribution of the viscous terms will be ignored.

Retaining terms only to order E, Eqs. (9a) and (9b) simplify to

$$\frac{\partial}{\partial r} (r^2 u) = 0 \quad (37a)$$

$$E \frac{\partial u}{\partial t} + u \frac{\partial u}{\partial r} + \frac{\partial p}{\partial r} = 0 \quad (37b)$$

The particle velocity follows immediately from Eq. (37a) to be

$$u(r, t; E) = -\frac{G(t; E)}{r^2} \quad (38)$$

where $G(t; E)$ is an arbitrary function of integration. Substituting Eq. (38) into (37b) and integrating with respect to the radial coordinate r yields

$$\frac{E \dot{G}}{r} + \frac{|G|G}{2r^4} + p = \tilde{f}(t) \quad (39)$$

where $\tilde{f}(t)$ is yet another arbitrary function of integration. The absolute value is imposed upon G to insure that particle jetting absorbs acoustic energy throughout the cycle.

The pressure $p(r, t)$ must satisfy the boundary conditions specified by Eqs. (10b) and (13b). Applying the boundary condition specified by Eq. (11b), it is clear that $\tilde{f}(t) = \cos(t)$. To apply the boundary condition specified by Eq. (13b), Eq. (39) must first be differentiated with respect to time with Eq. (13b) substituted for $\partial p / \partial t$ ($r=1, t$) to yield,

$$E \left[\ddot{G} + \left(\frac{2\pi L_e^* c^{*2}}{v^* \omega^{*2}} \right) \dot{G} \right] + |G| \dot{G} = -\sin(t) \quad (39a)$$

Because Eq. (39a) is nonlinear, it is not possible to readily identify its resistive and reactive components.

The solution to Eq. (39a) describes the time behavior of the particle velocity entering the cavity. It is not possible to seek approximate solutions by expanding $G(t;E)$ in powers of E . This kind of approach becomes singular for values of $t = (2n-1)\pi/2$, $n=0, +1, +2, \dots$. To illustrate this, the function $G(t;E)$ is expanded in powers of E , the first two terms of which are

$$G(t;E) = G_0(t) + EG_1(t) + O(E^2) \quad (40)$$

Substituting Eq. (40) into Eq. (39a) yields the following approximate solutions

$$G_0(t) = \sqrt{2 \cos(t)}; \quad G_1(t) \approx \frac{1}{2} \tan(t) - \left(\frac{2\pi L_e^* c^{*2}}{V^* \omega^{*2}} \right) \left(t + t^3/6 \right) \quad (41)$$

It is clear that the solutions $G_0(t)$ and $G_1(t)$ are not valid near $t = (2n-1)\pi/2$; they are valid only near $t = 2\pi n$. The methods of singular perturbation theory will be used to remove the singularity resulting in an approximate solution valid throughout the entire cycle (recall that Ingard and Ising's hot-wire measurements showed the oscillating orifice velocity to be symmetrical over each half-cycle). The procedures for deriving the approximate solution are (1) the solution given by Eq. (39) will be assumed to be valid only over the part of the half-cycle defined by $(4n-1/2)\pi/2 < t < (4n+1/2)\pi/2$, (2) a second approximate solution will be derived valid for the part of the half-cycle defined by $(4n-1)\pi/2 < t < (4n-1/2)\pi/2$ and $(4n+1/2)\pi/2 < t < (4n+1)\pi/2$ and (3) a third approximate solution will be derived valid in the very thin (in time) region near $t = (2n\pm 1)\pi/2$. The method of singular perturbation theory will be used to derive the third solution. Finally, with the approximate solution valid throughout the half-cycle range $(4n-1)\pi/2 \leq t \leq (4n+1)\pi/2$, the Fourier coefficients a_1 and b_1 will be calculated. The Fourier coefficients will then be used to predict resonator impedance.

Following this procedure, the details of which are summarized in Appendix A, the approximate solution to $G(t;E)$ is

$$G(t;E) \approx \left\{ \begin{array}{l} \sqrt{2 \cos(t)} + E \left[\frac{1}{2} \tan(t) - \left(\frac{2\pi L_e^* c^{*2}}{V^* \omega^{*2}} \right) (t+t^3/6) \right]; \\ \quad (4n-\frac{1}{2})\frac{\pi}{2} \leq t \leq (4n+\frac{1}{2})\frac{\pi}{2} \\ \\ \sqrt{2 \sin(\tau)} \pm E \left[\frac{\cot(\tau)}{2} - 2 \left(\frac{2\pi L_e^* c^{*2}}{V^* \omega^{*2}} \right) \left(\frac{0.59}{\sqrt{\tau}} \left(1 + \frac{\tau^2}{12} \right) - \left(\frac{\tau}{3} + \frac{\tau^3}{63} \right) \right) \right]; \\ \quad \tau = (4n+1)\frac{\pi}{2} \mp t; \quad 2^{1/3} E^{2/3} \leq \tau \leq \frac{\pi}{4} \\ \\ 2^{2/3} E^{1/3} Y_0^\pm(\eta) + 2^{5/6} E^{2/3} Y_1^\pm(\eta); \\ \\ \eta = \frac{(4n+1)\frac{\pi}{2} \mp t}{2^{1/3} E^{2/3}}; \quad 0 \leq \eta \leq 2. \end{array} \right. \quad (42)$$

where $Y_0^\pm(\eta)$ and $Y_1^\pm(\eta)$ are special functions defined in Appendix A. The solution described by Eq. (42) is used to calculate the Fourier harmonic coefficients a_1 and b_1 where

$$a_1(E) \approx 1.57 + 0.19 E^{5/3} + O(E^2) \quad (43a)$$

and

$$b_1(E) \approx E \left[0.07 - 0.43 \ln(E) - \left(\frac{2\pi L_e c^2}{V\omega^2} \right) (2.55 - 2.63 E^{1/3}) \right] \quad (43b)$$

With the harmonic components a_1 and b_1 specified, the resulting harmonic component of the acoustic particle velocity, written in complex notation where again it is understood that only the real part has physical meaning, is

$$u(r,t;E) = - \frac{G(t;E)}{r^2} = - \frac{e^{it}}{r^2} \left[a_1(E) - i b_1(E) \right] \quad (44)$$

The relationship between the amplitudes and relative phase of the incident and cavity sound pressure fields are determined by combining Eqs. (44) and (13b). The ratio of the cavity-to-incident sound pressure amplitudes and relative phase is respectively

$$\left| \frac{P_c^*}{P_i^*} \right| = \left| \left(\frac{2\pi L_e^* c^{*2}}{V^* \omega^{*2}} \right) E u \right| \approx 1.57 E \left(\frac{2\pi L_e^* c^{*2}}{V^* \omega^{*2}} \right) \quad (45a)$$

and

$$\phi_{ic} = -\phi_{ci} = -\tan^{-1} \left(\frac{a_1}{b_1} \right) \approx -\tan^{-1} \left\{ \frac{1.57 [1+0.1 E^{5/3}]}{E [0.07 - 0.43 \ln(E) - \left(\frac{2\pi L_e^* c^{*2}}{V^* \omega^{*2}} \right) (2.55 - 2.63 E^{5/3})]} \right\} \quad (45b)$$

Recalling that $E = \sqrt{\rho^* (\omega L_e^*)^2 / P_i^*}$ it is clear that for very high incident sound fields, $|P_c^*| \ll |P_i^*|$ and $\phi_{ci} \approx 90$ degrees. Further, the ratio $|P_c^*/P_i^*|$ should vary almost linearly with E ; the relative phase angle ϕ_{ci} , however, is a rather complicated function of the parameter E principally because of the term $\ln(E)$ in the denominator. In evaluating Eq. (45b), the term $-0.43 \ln(E)$ will never become excessively large because of the constraint that the amplitude of the incident sound field be small relative to the ambient pressure. Equation (45a) provides a convenient way to determine the characteristic length L_e^* . For E small;

$$\left| \frac{P_c^*}{P_i^*} \right| \approx 1.57 \left(\frac{2\pi L_e^* c^{*2}}{V^* \omega^{*2}} \right) \sqrt{\frac{\rho^* (\omega L_e^*)^2}{P_i^*}} = 1.57 \left(\frac{2\pi L_e^* c^{*2}}{V^* \omega^{*2}} \right) \sqrt{\frac{\rho^*}{P_i^*}} \quad (46)$$

Thus, measurements of $|P_c^*/P_i^*|$, P_i^* , and ω^* lead directly, via Eq. (46), to predictions of the characteristic length L_e^* . The details of these measurements are presented in Section 3. For the remainder of this derivation, L_e^* will be presumed to be known.

The resonator orifice area-averaged impedance follows immediately from its definition to yield

$$(-Z)_{ori} = \frac{1}{8} \left(\frac{d^*}{L_e^*} \right)^2 \left[\frac{a_1 + ib_1}{a_1^2 + b_1^2} \right] \quad (47)$$

where the term $1/8(d^*/L_e^*)^2$ references the particle velocity to the orifice inlet area $\pi d^{*2}/4$ instead of the reference hemispherical area $2\pi L_e^{*2}$. Substitution of Eq. (43a) and (43b) for a_1 and b_1 yields for the resonator resistance and reactance

$$(-R)_{ori} \approx 0.08 \left(\frac{d^*}{L_e^*} \right)^2 (1 - 0.1 E^{5/3}) \quad (48a)$$

and

$$(-X)_{ori} \approx \frac{0.05 \left(\frac{d^*}{L_e^*}\right)^2 E \left[0.07 - 0.43 \ln E - \left(\frac{2\pi L_e^* c^{*2}}{V^* \omega^{*2}}\right) (2.55 - 2.63 E^{1/3}) \right]}{[1 - 0.2 E^{5/3}]} \quad (48b)$$

For E sufficiently small, Eqs. (48a) and (48b) simplify to

$$(-R)_{ori} \approx 0.08 \left(\frac{d^*}{L_e^*}\right)^2 \quad (49a)$$

and

$$(-X)_{ori} \approx 0.05 \left(\frac{d^*}{L_e^*}\right)^2 E \left[0.07 - 0.43 \ln(E) - \left(\frac{2\pi L_e^* c^{*2}}{V^* \omega^{*2}}\right) (2.55 - 2.63 E^{1/3}) \right] \quad (49b)$$

Nondimensionalized with respect to the characteristic impedance $\rho^* c^*$, the resonator resistance and reactance are

$$\frac{(-R)_{ori}^*}{\rho^* c^*} \approx 0.08 \left(\frac{d^*}{L_e^*}\right)^2 \sqrt{\frac{P_i^*}{\rho^* c^{*2}}} \quad (50a)$$

and

$$\frac{(-X)_{ori}^*}{\rho^* c^*} \approx 0.05 \left(\frac{d^*}{L_e^*}\right) \left(\frac{\omega^* d^*}{c^*}\right) \left[0.07 - 0.43 \ln E - \left(\frac{2\pi L_e^* c^{*2}}{V^* \omega^{*2}}\right) (2.55 - 2.63 E^{1/3}) \right] \quad (50b)$$

Further interpretation of the nonlinear impedance as defined by Eqs. (50a) and (50b) is deferred until the experimental measurements leading to the definition of the characteristic length L_e^* are described in Section 3.

3. EXPERIMENTAL PROGRAMS

The two microphone method used by Dean¹ and others has been applied to measure the impedance of the resonator geometries summarized in Table I. As shown in the Table, the range of the three important test parameters (τ^*/d^* , d^*/D^* , d^*/L^*) were varied approximately one order-of-magnitude. The purpose of the measurement program is two-fold. First, it will be used to define experimentally the parameter K introduced in the derivation of the linear theory (Section 2.4) and the characteristic length L_e^* introduced in the derivation of the nonlinear theory (Section 2.5). Second, it will be used to improve and/or refine the model.

The two-microphone approach and the instrumentation required is described in Section 3.1 below. The application of the data to the linear and nonlinear regimes are described in Sections 3.2 and 3.3 respectively.

3.1 Measurement System

A schematic of the instrumentation and test set-up required to use the two-microphone method is shown in Figure 1. The resonator consists of a cylindrical cavity of diameter D^* , depth L^* , and an orifice of diameter d^* and thickness τ^* .

Dean derives the following expressions for the resonator orifice-area averaged resistance and reactance

$$\frac{R^*}{\rho^* c^*} = \left[10 \frac{\text{SPL}(i) - \text{SPL}(c)}{20} \right] \frac{\sin \phi_{ci}}{\sin\left(\frac{\omega^* L^*}{c^*}\right)} \left(\frac{d^*}{D^*}\right)^2 \quad (51a)$$

and

$$\frac{X^*}{\rho^* c^*} = - \left[10 \frac{\text{SPL}(i) - \text{SPL}(c)}{20} \right] \frac{\cos \phi_{ci}}{\sin\left(\frac{\omega^* L^*}{c^*}\right)} \left(\frac{d^*}{D^*}\right)^2 \quad (51b)$$

where $\text{SPL}(i) - \text{SPL}(c)$ represents the sound pressure level difference (in dB) between the incident sound field and the cavity sound field and ϕ_{ci} represents the corresponding phase difference. The two-microphone method of measuring impedance requires the simultaneous measurement of the incident and cavity sound pressure levels and phase. These measurements are obtained by flush mounting one microphone at the cavity base and the other flush with the wall containing the orifice as shown in Fig. 1. It is important to locate the incident microphone sufficiently far from the orifice to avoid near field effects (our experience shows that a separation distance of about 4 or 5 orifice diameters is adequate). The microphone should be located sufficiently close, however, so that the separation distance is small relative to the incident sound wavelength; this is necessary to insure accurate measurement of the incident sound wave amplitude and phase.

A schematic of the instrumentation used to conduct the experiments is shown in Figure 3. To generate incident sound pressure levels up to 160 dB, a JBL type 2480 driver capable of producing in excess of 10 watts of relatively "clean" acoustic power is used as the sound source. The 2" diameter driver throat is coupled to the test section by means of a 2" to 4" diameter exponential expansion, JBL type H-93. Sound pressure levels in excess of 150 dB exceed the input capability of the GR 1560-P42 preamp. A 10 dB microphone Attenuator, GR Type 1962-3200 has been added, which extends the measurement range accordingly.

The signal generated by the Heath 1G-18 audio generator is amplified by the McIntosh MC2100 100 watt/channel power amplifier to power the JBL driver. The audio generator provides a tracking signal for the AD-YU Synchronous Filter and phase meter system. The 1036 system filters the two microphone input signals to the tracking signal frequency ± 2.5 Hz. The AD-YU Type 524A4 Phase Meter reads phase angle between the signals independent of signal amplitudes. The phase angle output is displayed on the AD-YU Type 2001 digital volt meter. A General Radio-1564 1/10 octave filter together with a Heath Type IM2202 DVM is used to record the output signals from each of the two microphones. Also the two signals are observed on a Tektronix 533 Oscilloscope to visually note approximate phase and distortion effects.

The output of the incident microphone channel of the synchronous filter is used as a control voltage for an automatic level control amplifier. This control amplifier adjusts the drive level to the power amplifier in such a way as to keep the incident level constant, independent of frequency and amplitude response irregularities in the loudspeaker and tunnel.

As a convenience, a triple ganged 5 dB per step ladder attenuator is used to simultaneously increase the power amplifier drive level and decrease the synchronous filter input signals so that the control loop of the automatic level control amplifier always has the same gain. This has the added advantage keeping the levels at the AD-YU Filter input constant for all testing levels. Since the AD-YU Filter displays a small amplitude-phase dependency, this improves accuracy as well as speed of data acquisition. A test of both microphones mounted flush in the wind tunnel wall showed phase tracking within $\pm .2^\circ$ over a sound pressure level range of 70-150dB.

3.2 Linear Regime

3.2.1 The $\epsilon=0$ Case

At resonance, the response of the cavity to the incident sound pressure field was shown in Eq. (28c) to be proportional to the square root of the Reynolds number

$$\left| \frac{P_c^*}{P_i^*} \right|_{\text{res}} \approx K^{-1} \sqrt{\frac{\omega_{\text{res}}^* L_e^{*2}}{\nu^*}} ; L_e^* = \frac{d^{*2}}{8d_e^*} \quad (28a)$$

The only unknown in the above equation is the parameter K. Accordingly, tests were conducted to determine K experimentally. The test procedure was straight-forward. Only those resonator geometries that satisfied the constraint that $\epsilon < 0.1$ were considered (recall that $\epsilon = 64 \left(\frac{d_e^*}{d^*}\right)^2 \left[\frac{P_c^*}{P_i^*} (\omega d^*)^2\right]$ - the particular value $\epsilon < 0.1$ will be explained later). The geometry of the resonators tested are summarized in Table II. The various values of K tabulated were determined by measuring $|P_c^*/P_i^*|_{res}$ at resonance for an incident sound pressure amplitude of 70dB. An approximate fit to the data is

$$K \approx \frac{0.8}{1+3(\tau^*/d^*)} \quad (52)$$

Figure 4 shows $|P_c^*/P_i^*|_{res}$ to be predicted to within 10% accuracy using Eq. (52) to predict K.

With K specified by Eq. (52), the final approximate expression for resonator impedance, written in *dimensional* terms, is

$$(-Z)_{ori}^* \approx \underbrace{\left[\frac{6.4 \left(\frac{d_e^*}{d^*}\right)^2}{1+3\left(\frac{\tau^*}{d^*}\right)} \sqrt{\rho^* \mu^* \omega^*} \right]}_{\text{Resistance}} + i \underbrace{\left[\rho^* \omega^* d_e^* - \frac{\rho c^{*2} S^*}{V^* \omega^*} \right]}_{\text{Reactance}} \quad (53)$$

where (d_e^*/d^*) is defined by Eq. (24) and $S^* = \pi d^2/4$. Assuming radiation resistance to be negligible and $d^*/D^* < 1$, the resistance as predicted by the real part of Eq. (53) differs from that predicted by Eq. (1) by less than 10% over the range of resonator orifice geometries satisfying $0.5 < \tau^*/d^* < 1.5$. A comparison between predicted and experimental resistance measurements is shown in Figure 5. The errors associated with predicting resistance from Eq. (53) arise from two separate sources, those associated with the parameter K and those associated with the ratio (d_e^*/d^*) . As shown in Figure 5, Eq. (53) can be used to predict the linear value of resistance to within an accuracy of roughly 10%.

Equation (53) can also be used to predict the off-resonance behavior of resonators. Following the procedures described in Section 2.4.1, the ratio of the cavity-to-incident sound pressure amplitudes $|P_c^*/P_i^*|$ and relative phase angles ϕ_{ci} can be shown to be

$$\left| \frac{P_c^*}{P_i^*} \right| = \frac{\left(\frac{\omega_{res}^*}{\omega^*}\right)^2}{\sqrt{\left(\frac{K}{\sqrt{Re}}\right)^2 + \left[1 - \left(\frac{\omega_{res}^*}{\omega^*}\right)^2\right]^2}} \quad (54a)$$

$$\phi_{ci} = \tan^{-1} \left[\frac{\frac{K}{\sqrt{Re}}}{1 - \left(\frac{\omega_{res}^*}{\omega^*}\right)^2} \right] \quad (54b)$$

where K is defined by Eq. (52) and $\omega_{res}^* = c^* S^* / V d \epsilon^*$. Figures 6 and 7 summarize respectively the comparison between predictions based on using Eqs. (54a) and (54b) and measured data. As shown in the Figures, the comparison is excellent.

3.2.2 Weakly Nonlinear Case

Measurements of the weakly nonlinear resistance and reactance of five resonators are summarized in Figures 8 and 9 respectively. The nondimensionalized resistance data can be divided into two regimes, one in which the resistance is virtually independent of incident sound pressure amplitude (say $\epsilon < 0.1$ - this is the reason only $\epsilon < 0.1$ data was considered in determining the parameter K in Section 3.2.1) and the other strongly dependent upon it. For $\epsilon > 0.5$, the resistance values appear to converge into a behavior dependent only upon the nonlinear parameter ϵ . This is in agreement with the behavior predicted from the model governing equation (see Eq. 18a). The damping or loss term in Eq. (18a), the coefficient of \dot{F} , is $(K/\sqrt{Re} + \epsilon|F|)$. At very low values of ϵ , the first term dominates in accord with the data shown in Fig. 8. For sufficiently large values of ϵ , the nonlinear term $\epsilon|F|$ dominates and one would expect the importance of the individual resonator parameters (τ^*, d^*, D^*, L^*) to become unimportant. This is explicitly shown below in the following empirical curve fit to the data summarized in Fig. 8,

$$\left[\frac{R^*}{\rho^* \omega^* L \epsilon^*} \right]_{res} \approx \sqrt{\left[\frac{K}{\sqrt{Re}} \right]^2 + 8 \left(\frac{d \epsilon^*}{d} \right)^2 + 0.42 \epsilon + 0.61 \epsilon^2} \quad (55)$$

where $8(d\epsilon^*/d)^2 K/\sqrt{Re}$ represents the orifice area based non-dimensionalized resonator resistance at $\epsilon=0$. Equation (55) differs negligibly from the real part of Eq. (33a), derived on the basis of a regular perturbation expansion for values of $\epsilon < 0.01$. For large values of ϵ , however, Eq. (55) matches considerably more accurately, the measured data as shown in Figure 8.

According to Eq. (33a), the nondimensionalized reactance data should *decrease* with *increasing* incident sound pressure level from its tuned resonance value of zero at $\epsilon=0$. The decrease should be only a function of the nonlinear parameter ϵ ,

$$\left[\frac{-X^*}{\rho^* \omega^* d \epsilon^*} \right]_{res} \approx -\frac{4\epsilon}{9\pi} \quad (56)$$

The measured reactance data is summarized in Fig. 9. Despite the scatter in the data which arises because of the extreme sensitivity of the cosine function near ninety degrees (recall that at resonance, $\phi_{ci}=90$ degrees), the nondimensionalized reactance data is roughly dependent only upon the nonlinear parameter ϵ . The model

prediction Eq. (56) is seen in Fig. 9 to over predict the measurements. As shown in Fig. 9, a "better" fit to the data is

$$\left[\frac{X^*}{\rho^* \omega^* d_e^*} \right]_{res} \approx - \frac{\epsilon}{9\pi} \quad (57)$$

In agreement with the resistance data shown in Fig. 8, nonlinear effects are not important for $\epsilon < 0.1$.

The main findings of this study is that the onset of acoustic nonlinearity occurs only when the parameter $\epsilon > 0.1$ where $\epsilon = 64 \left(\frac{d_e^*}{d^*} \right)^2 \left[\frac{P_i^*}{\rho^* (\omega^* d^*)^2} \right]$. Significant deviations from its linear or $\epsilon = 0$ values do not occur until $\epsilon > 0.2$.

3.3 Nonlinear Regime

The derivation of the nonlinear model described in Section 2.5 assumed the characteristic length L_e^* was independent of both incident sound pressure level and frequency. Equation (46) provides a convenient way to indirectly measure its value. Rewriting it in terms of the resonator resonant frequency defined by Eq. (23a),

$$\left| \frac{P_c^*}{P_i^*} \right| \approx 12.56 \left(\frac{L_e^*}{d^*} \right)^2 \left(\frac{\omega_{res}^*}{\omega^*} \right) \sqrt{\frac{\rho^* (\omega_{res}^* d_e^*)^2}{P_i^*}} \quad (58)$$

At resonance, where $\omega = \omega_{res}^*$, the ratio $|P_c^*/P_i^*|$ becomes, only a function of the amplitude of the incident sound pressure field. Measurements of the ratio $|P_c^*/P_i^*|_{res}$ vs $\sqrt{\rho^* (\omega_{res}^* d_e^*)^2 / P_i^*}$ are summarized in Figure 10. Although the slopes of the $|P_c^*/P_i^*|_{res}$ vs $\sqrt{\rho^* (\omega_{res}^* d_e^*)^2 / P_i^*}$ data appear to be constant, they do exhibit slight variations with resonator geometry. Comparing the data shown in Fig. 10 with Eq. (58) yields the following estimate of the characteristic length (L_e),

$$\frac{L_e^*}{d^*} \approx 0.26 \left[1 + \frac{1}{9} \left(\frac{\tau^*}{d^*} \right) \right] \quad (59)$$

The characteristic length defined by Eq. (59) should be viewed with caution because of the extremely limited data base used in its determination. For example, the ratio $d^*/D^* < 1$ for all of the resonator configurations shown in Fig. 10.

The derivation leading to Eq. (59) assumes that the characteristic length (L_e^*/d^*) is independent of frequency. If this is true, then the ratio $|P_c^*/P_i^*|$ should vary inversely with frequency as predicted by Eq. (58). To verify this, the frequency of the resonator geometry having $D^* = 1.905$ cm, $L^* = 2.54$ cm, $\tau^* = .051$ cm, $d^* = .091$ cm

(the \circ symbol in Fig. 10) was varied from about 300 Hz to 650 Hz and the corresponding ratios $|P_C^*/P_i^*|$ measured. A comparison between measurements of $|P_C^*/P_i^*|$ and predictions based on combining Eqs. (58) and (59) is shown in Fig. 11. The excellent agreement between prediction and measurement shown verifies that (L_e^*/d) is independent of both sound pressure level and frequency. With the characteristic length L_e^* specified by Eq. (59), the final form of the resonator resistance and reactance follows immediately from Eqs. (50a) and (50b). Nondimensionalized with respect to $\rho^* \omega^* d^*$, they are

$$\left[\frac{-R^*}{\rho^* \omega^* d^*} \right] \approx \frac{1.17}{\left[1 + \frac{1}{9} \left(\frac{\tau^*}{d^*} \right)^2 \right]} \sqrt{\frac{P_i^*}{\rho^* (\omega^* d^*)^2}} \approx \frac{0.31}{E \left[1 + \frac{1}{9} \left(\frac{\tau^*}{d^*} \right)^2 \right]} \quad (60)$$

$$\left[\frac{-X^*}{\rho^* \omega^* d^*} \right] \approx \frac{0.19}{\left[1 + \frac{1}{9} \left(\frac{\tau^*}{d^*} \right)^2 \right]} \left\{ 0.07 - 0.43 \ln E - 2.09 \left(\frac{d_e^*}{d^*} \right) \left(\frac{\omega_{res}^*}{\omega^*} \right)^2 \left[1 + \frac{1}{9} \left(\frac{\tau^*}{d^*} \right)^2 \right] (2.55 - 2.63 E^{1/3}) \right\} \quad (61)$$

The nondimensionalized form of Eqs. (60) and (61) show explicitly their dependence upon the parameter E and resonator geometry. A comparison between predicted and measured resistance and reactance is shown in Fig. 12 for five different resonator geometries. The reactance of each configuration is "tuned" to zero at an incident sound pressure level of 70 dB by proper adjustment of the sound frequency. The resistance, as predicted by Eq. (60), is in excellent agreement with the data, thus confirming the assumptions made in its derivation. The reactance, as predicted by Eq. (61), is also in close agreement with data as shown in Fig. 12. Also shown in Fig. 12 is the close agreement between predicted (via combining Eqs. (45b) and (59)) and measured relative phase between the incident and cavity sound fields.

As a final verification of the model, the predicted resistance, reactance and relative phase variation with sound frequency is compared with measurements in Fig. 13. The incident sound pressure level was maintained at 140 dB and the frequency varied from about 300 Hz to 650 Hz. The measured phase change with frequency was larger than predicted. For example, between 300 and 650 Hz, the measured phase increased from 76 to 97 degrees, a 21 degree phase change, while the corresponding predicted phase change is only about 9 degrees. The same trend was observed for the reactance. Here the reactance data varied from approximately -2 at 300 Hz to +0.5 at 650 Hz in contrast with the predicted variation of -1.4 at 350 Hz to -0.06 at 650 Hz. Part of these differences may be related to nonsinusoidal wave form of the cavity sound field. Observations on the oscilloscope showed the cavity wave form to be highly distorted when the incident sound pressure level was 140 dB

(the corresponding cavity sound pressure level was 129 dB at 404 Hz). Oscilloscope traces of the incident sound pressure showed it to be reasonably sinusoidal. The measured cavity phase may contain contributions to the fundamental harmonic frequency arising from nonlinear interactions not accounted for in the nonlinear model. Since reactance is proportional to the $\cos \phi$, these nonlinear induced small errors in phase (e.g. from Fig. 13, +4.6% error at $f = 300$ Hz and -88% error at $f = 650$ Hz), strongly amplified near 90 degrees, may account for the differences in predicted and measured values shown in Fig. 13. Figure 13 also shows that both predicted (Eq. 60) and measured resistance are independent of frequency. Since the resistance is proportional to $\sin \phi$, the errors in phase near 90 degrees are unimportant. This explains the excellent agreement between predicted and measured resistance.

In reducing the data, care was taken to account for two serious sources of measurement error. One is phase and amplitude distortion of the cavity sound field due to impingement upon the cavity microphone by the particle velocity (see Fig. (1) during inflow. The second is flexure of the face plate due to the excessively high incident SPL's. A detailed accounting of these effects is summarized in Appendix B. To ensure that the relative phase measurements were unaffected by temperature increases due to the high SPL levels, a thermister probe was installed in the cavity. Temperature measurements showed negligible changes - less than 2 degrees Fahrenheit for values of P_i between 70 and 160 dB.

The experimentally determined characteristic length (L_e^*) provides direct information on the value of the discharge coefficient C_D which connects the maximum particle velocity jetting at the orifice vena contracta to its orifice area-averaged value. The spherical inflow model forces the maximum vena contracta particle velocity to occur at the hemispherical surface $2\pi L_e^{*2}$. It follows, via the continuity of particle volume flow velocity, that

$$q_{\max}^* \cdot 2\pi L_e^{*2} = \frac{q_{\text{ori}}^* \cdot \pi d^{*2}}{4} \longrightarrow C_D = \frac{q_{\text{ori}}^*}{q_{\max}^*} = 8 \left(\frac{L_e^*}{d^*} \right)^2$$

Substituting Eq. (59) for the ratio L_e^*/d^* yields

$$C_D \approx 0.545 \left[1 + \frac{2}{9} \left(\frac{\tau^*}{d^*} \right) \right] \quad (62)$$

a value remarkably close to that measured by orifices exposed to steady-state flow (see e.g., Fig. E-1 of the study by Rogers and Hersh¹²).

* It is clear from a comparison between Eqs. (60) and (61) that $|R| \gg |X|$ regardless of the frequency of the incident sound (the constraint that $E \ll 1$ restricts the maximum value of the frequency).

Thus, from a sound absorption application viewpoint, Helmholtz resonators operate as broadband absorbers in the high SPL range. To clarify this, consider a wall containing an array of Helmholtz resonators exposed to intense sound. The driving sound field consists of both incident and reflected waves. The fraction of incident acoustic energy (α) absorbed by the Helmholtz resonators is a function of the wall impedance and may be written¹³

$$\alpha = \frac{4 \left[\frac{(R)_{ori}^*}{\rho^* c^* \sigma} \right]}{\left[\frac{(R)_{ori}^*}{\rho^* c^* \sigma} + 1 \right]^2 + \left[\frac{(X)_{ori}^*}{\rho^* c^* \sigma} \right]^2} \quad (63)$$

Equations (60) and (61) rewritten in terms of $\rho^* c^*$ may be used to estimate $(R)_{ori}^*/\rho^* c^*$ and $(X)_{ori}^*/\rho^* c^*$. The quantity $\sigma = (d/D)^2$ is the total orifice open area to cavity area ratio (for cylindrical cavities). It is assumed that the array of Helmholtz resonators are sufficiently far apart from their neighbors so that they respond independently. Since $(R)_{ori}^*/\rho^* c^*$ is independent of frequency (see Fig. 13), and $|(R)_{ori}^*/\rho^* c^* \sigma| \gg |(X)_{ori}^*/\rho^* c^* \sigma|$, it is clear that the absorption coefficient (α) is very insensitive to frequency. It follows that Helmholtz resonators exposed to intense sound are broadband sound absorbers. This is in sharp contrast to their behavior at low sound amplitudes where generally $|R/\rho c| \ll |X/\rho c|$ except near resonance.

The use of Eqs. (60) and (61) in sound absorption calculations is not straight forward. The complexity arises in specifying the incident driving sound amplitude P_i^* . With regard to the above application of a sound wave reflecting from a wall containing an array of Helmholtz resonators, the proper incident driving pressure amplitude is $P_i^* + P_r^*(P_i^*)$. Here the reflected sound field $P_r^*(P_i^*)$ is written explicitly as a function of the incident sound to emphasize the nonlinearity of the Helmholtz wall impedance $Z^*(P_i^* + P_r^*)$,

$$\frac{P_i^* + P_r^*(P_i^*)}{u_i^* + u_r^*(P_i^*)} = \frac{Z^*[P_i^* + P_r^*(P_i^*)]}{\sigma} \quad (64)$$

The quantity $[Z^*(P_i^* + P_r^*)]$ is the orifice-area averaged impedance, σ is the percent open area defined earlier and u_i^* and $u_r^*(P_i^*)$ are the incident and reflected sound particle velocities respectively (far from the orifice). Assuming that P_i^* and $P_r^*(P_i^*)$ are plane waves, the particle velocities are related to their driving pressure fields as

$$P_i^* = \rho^* c^* u_i^* \quad \text{and} \quad P_r^*(P_i^*) = -\rho^* c^* u_r^*(P_i^*)$$

Substituting these velocity fields into Eq. (64) and solving for the ratio $P_r^*(P_i^*)/P_i^*$ yields

$$\frac{P_r^*(P_i^*)}{P_i^*} = \frac{[(R)_{ori}^*/\rho^*c^*\sigma - 1] + i[(X)_{ori}^*/\rho^*c^*\sigma]}{[(R)_{ori}^*/\rho^*c^*\sigma + 1] + i[(X)_{ori}^*/\rho^*c^*\sigma]} \quad (65)$$

To correctly specify P_r^* , an iterative approach to solving Eq. (65) is required. For example, assume that the driving pressure is the incident sound pressure P_i^* . Substitute P_i^* into Eq. (65) to predict P_r^* . Then replace P_i^* by $P_i^* + P_r^*$ and substitute this value back into Eq. (65) to obtain a revised estimate of P_r^* . Repeat this process until P_r^* becomes virtually constant. In this application, the correct driving sound pressure amplitude incident to the resonator orifice is $P_i^* + P_r^*(P_i^*)$. This value of the driving pressure amplitude would be used in calculating the parameter E in Eqs. (60) and (61). With regards to interpreting the data shown in Figures 10-13, the proper incident driving pressure amplitude is $2P_i^*$ corresponding to pressure doubling at the incident hard wall microphone location (see Fig. 1). By locating the incident microphone far from the resonator orifice, the complexities described above have been avoided.

4. CONCLUSIONS

The acoustic behavior of Helmholtz resonators has been divided into three categories corresponding to (1) very weak, (2) moderately weak and (3) very intense incident sound pressure amplitude. The first two categories are characterized by a "linear" or almost "linear" impedance and the third by a "nonlinear" impedance. The "linear" and almost "linear" regimes are defined by the small parameter ϵ expressed below in terms of the resonator geometry, incident sound pressure amplitude P_i^* and circular frequency ω^* , as

$$\epsilon = 64 \left[\frac{\tau^*}{d^*} + \frac{0.85}{1 + 0.625 \left(\frac{d^*}{D^*} \right)} \right]^2 \left[\frac{P_i^*}{\rho^* (\omega^* d^*)^2} \right]$$

The quantities τ^* and d^* represent the orifice thickness and (circular) diameter respectively; D^* is the (cylindrical) cavity diameter. The corresponding nondimensionalized orifice area-averaged resistance and reactance at resonance are defined empirically by Eqs. (55) and (57), rewritten below in a slightly more convenient form, as

$$\frac{(R)_{res}^*}{\rho^* c^*} \approx \sqrt{\frac{0.64 \omega^* \nu^*}{c^{*2} \left[1 + 3 \left(\frac{\tau^*}{d^*} \right)^2 \right] c_D^2} + \left(\frac{P_i^*}{\rho^* c^{*2}} \right) (0.42 + 0.61 \epsilon)}$$

$$\frac{(X)_{res}^*}{\rho^* c^*} \approx \frac{1}{c_D} \left(\frac{\omega^* d^*}{c^*} \right) \left[\frac{\tau^*}{d^*} + \frac{0.85}{1 + 0.625 \left(\frac{d^*}{D^*} \right)} \right] \frac{\epsilon}{9\pi}$$

where C_D is the Reynolds number dependent orifice discharge coefficient defined by Eq. (26). Both data and model prediction show that the effects of weak nonlinearity are to *increase* resistance and *decrease* reactance. The model shows resistance to arise from two sources, one being viscous losses that are independent of particle velocity and the other convective inertial losses that are linearly proportional to particle velocity. The decrease in reactance arises from a reduction of the orifice effective inertia length (d_e^*). In accord with the conclusions of Ingard and Ising, the reduction of d_e^* is believed to be related to particle velocity jetting generated by the fluid nonlinear inertia. It is clear that, providing ϵ is small, both the resistance and reactance depend weakly upon the sound amplitude P_i^* . Significant deviations of the impedance from its "linear" or $\epsilon=0$ value do not occur until $\epsilon > 0.2$. As an example, consider a cavity-backed resonator with $d^* = 1.5 \times 10^{-3}$ meters (~ 0.06 "), $\tau^*/d^* = 0.2$ and ($d^*/D^* \sim 0.1$) exposed to an incident sound field at 1,000 Hz. Significant deviations occur when the incident sound pressure level is equal to or greater than about 85 dB.

The nonlinear regime is defined by the small parameter E expressed below in terms of the resonator geometry and incident sound field as

$$E = 0.26 \left[1 + \frac{1}{9} \left(\frac{\tau^*}{d^*} \right) \right] \sqrt{\frac{\rho^* (\omega^* d^*)^2}{P_i^*}}$$

Using the same resonator geometry and frequency as described above, nonlinear effects become important when the incident sound pressure level is equal to or greater than about 130 dB. The corresponding resistance and reactance follow from Eqs. (60) and (61) rewritten below as

$$\left[\frac{R^*}{\rho^* c^*} \right] \approx \frac{1}{1.57 C_D} \sqrt{\frac{P_i^*}{\rho^* c^{*2}}}$$

and

$$\left[\frac{X^*}{\rho^* c^*} \right] \approx \frac{(\omega^* d^*)}{(1.57)^2 \sqrt{8 C_D}} \left\{ 0.07 - 0.43 \ln E - a (2.55 - 2.63 E^{1/3}) \right\}$$

where

$$a = 2.09 \left[1 + \frac{1}{9} \left(\frac{\tau^*}{d^*} \right) \right] \left[\frac{\tau^*}{d^*} + \frac{0.85}{1 + 0.625 \left(\frac{d^*}{D^*} \right)} \right] \left(\frac{\omega^*_{res}}{\omega^*} \right)^2$$

$$\text{and } C_D \approx 0.545 \left[1 + \frac{2}{9} \left(\frac{\tau^*}{D^*} \right) \right]$$

is the orifice high SPL discharge coefficient. The resistance is shown both theoretically and experimentally to be independent of frequency and proportional to the square root of the incident sound amplitude. Since $|R/\rho c| \gg |X/\rho c|$, Helmholtz resonators absorb sound in a broadband manner in contrast to its narrowband sound absorption at low pressure levels.

REFERENCES

1. Lord Rayleigh: Theory of Sound - 1945 (reissue) New York, Dover Publications.
2. Junger, M.C., "Helmholtz Resonators in Load-Bearing Walls", Noise Control Engineering, Vol. 4, No. 1, 17-25, Jan-Feb, 1975.
3. Crandall, I. B., Theory of Vibrating Systems and Sound, New York, D. Van Nostrand & Co., 1927.
4. Ingard, U., "On the Theory and Design of Acoustical Resonators", J. Acoust. Soc. Am., V. 25, 1037-1062, 1953.
5. Sivian, L. J. "Acoustic Impedance of Small Orifices", Acoust. Soc. Am., V. 7, 94-101, 1935.
6. Melling, T. H., "The Acoustic Impedance of Perforates at Medium and High Sound Pressure Levels," Jour. Sound & Vib., V. 29, no. 1, 1-65, 1973.
7. Ingard, U. and Ising, H., "Acoustic Nonlinearity of an Orifice", J. Acoust. Soc. Am., Vol. 42, No. 1, 6-17, 1967.
8. Sirignano, W. A., "Non Linearita dei Risonatori di Helmholtz", Aerotecnica Missili E. Spazio N., 4-1972.
9. Zinn, B. T., "A Theoretical Study of Nonlinear Damping by Helmholtz Resonators", Preprint No. 69-481, AIAA 5th Propulsion Specialists Meeting, June 1966.
10. Hersh, A. S. and Rogers, T, "Fluid Mechanical Model of the Acoustic Impedance of Small Orifices", NASA CR-2682, May 1966.
11. Dean, P. D., "An In Situ Method of Wall Acoustic Impedance Measurements in Flow Ducts", J. Sound Vib., Vol. 34, No. 1, 1974, 97-130.
12. Rogers, T. and Hersh, A. S., "Effect of Grazing Flow on Steady-state Resistance of Isolated Square-Edged Orifices", NASA CR-2681, April, 1976.
13. Kinsler, L. E. and Frey, A. R., Fundamentals of Acoustics, 2nd Ed., John Wiley & Sons, Pub., 1962, ch. 6, p. 133.

TABLE I. SUMMARY OF RESONATOR GEOMETRIES TESTED

D^* (cm)	L^* (cm)	d^* (cm)	τ^* (cm)	(τ^*/d^*)	(d^*/D^*)	(d^*/L^*)
1.905	1.27	0.091	0.025	0.278	0.048	0.072
	1.27	0.091	0.051	0.558	0.048	0.072
	2.54	0.091	0.025	0.278	0.048	0.036
	2.54	0.178	0.102	0.573	0.093	0.070
	2.54	0.356	0.102	0.286	0.187	0.140
	2.54	0.114	0.051	0.071	0.375	0.281
	2.54	0.178	0.051	0.286	0.093	0.070
	5.08	0.178	0.051	0.287	0.093	0.036
	5.08	0.356	0.051	0.143	0.187	0.070
3.175	1.27	0.091	0.025	0.278	0.029	0.072
	2.54	0.178	0.025	0.140	0.056	0.070
		0.356	0.025	0.070	0.112	0.140
			0.051	0.143		
			0.102	0.278		
			0.203	0.570		
			0.406	1.140		
		0.714	0.051	0.071	0.225	0.281
			0.102	0.143		
			0.203	0.284		
5.08	2.54	0.714	0.102	0.143	0.141	0.281
	3.81	0.714	0.102	0.143	0.141	0.187

TABLE II. SUMMARY OF RESONATOR DATA USED TO DETERMINE PARAMETER K

d^* (cm)	τ^* (cm)	L^* (cm)	D^* (cm)	f_{res} (Hz)	$ P_C^*/P_i^* _{max}$ (measured)	K	$ P_C^*/P_i^* $ (predicted)
0.178	0.025	1.270	1.905	1058	8.97	.552	8.84
"	0.051	2.540	"	682	7.78	.444	8.02
"	"	3.810	"	561	7.12	.440	7.27
"	"	5.080	"	476	7.07	.408	6.70
0.356	0.025	2.540	"	1153	17.44	.673	17.82
"	"	"	3.175	697	13.21	.665	13.32
"	0.051	"	1.905	1097	16.97	.622	18.85
"	"	3.810	"	880	16.16	.585	16.88
"	"	5.080	"	746	16.11	.540	15.54
"	"	2.540	3.175	663	14.64	.541	14.13
"	"	4.445	"	494	13.55	.504	12.20
0.714	0.025	3.810	5.080	504	22.96	.691	21.99

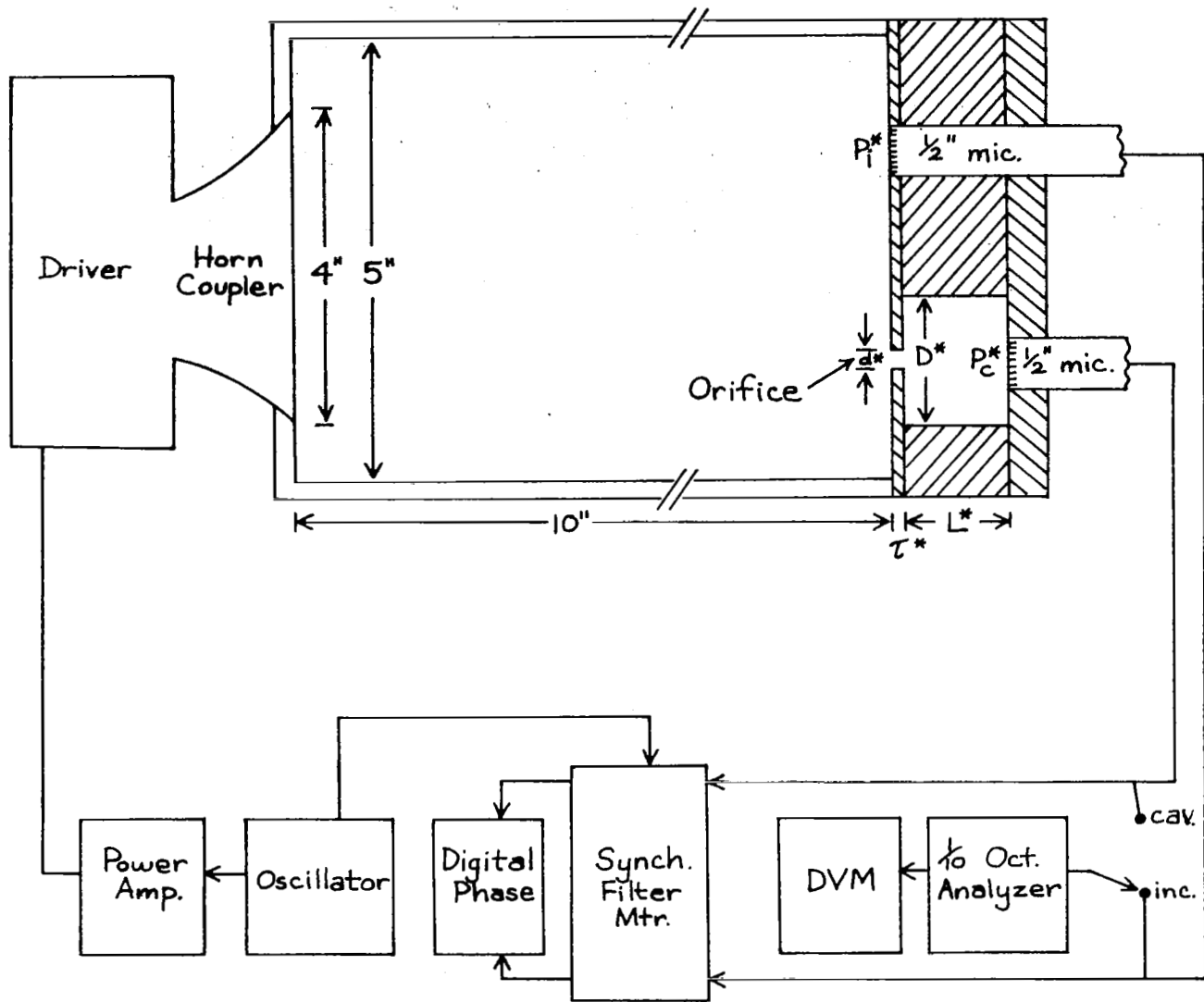


FIGURE 1. SCHEMATIC OF TWO-MICROPHONE MEASUREMENT SYSTEM

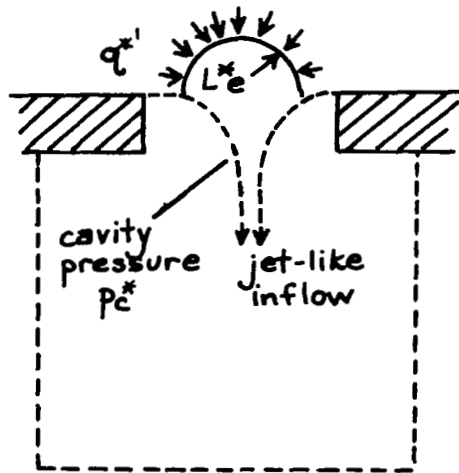
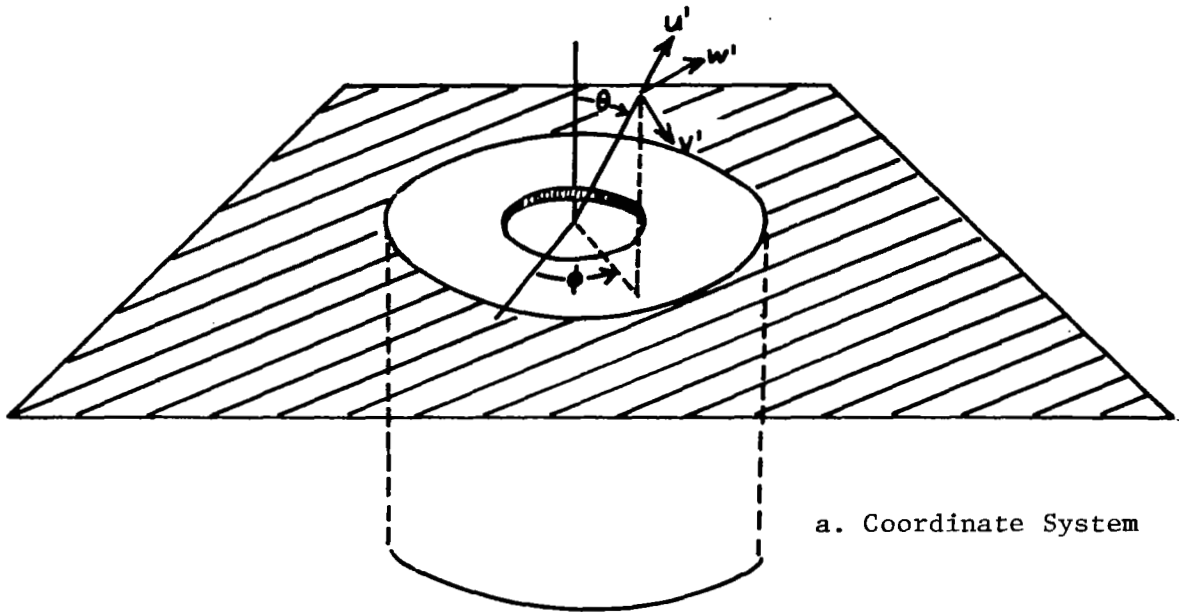


FIGURE 2. DEFINITION OF SOUND PARTICLE COORDINATE SYSTEM

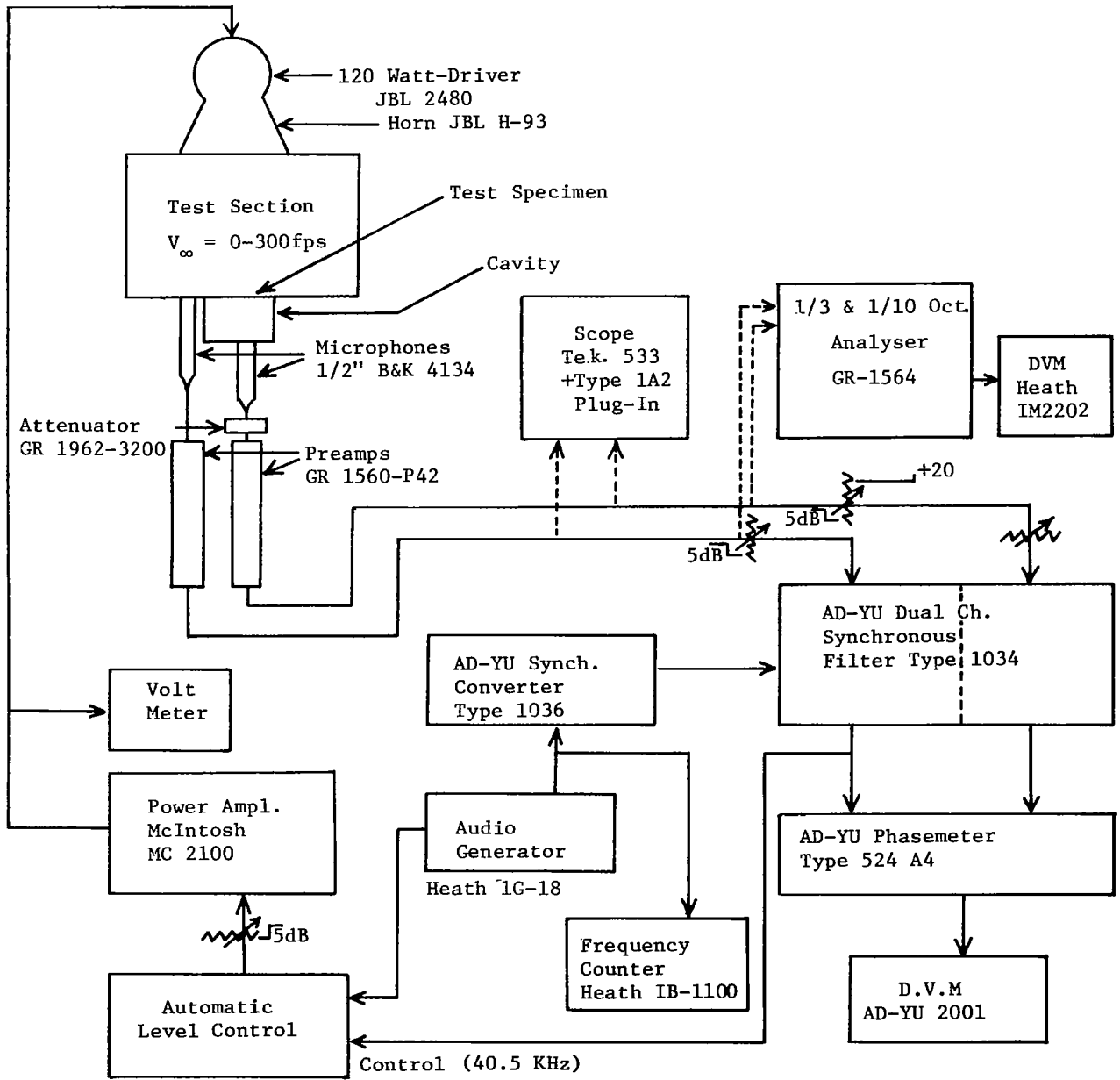


FIGURE 3. TWO-MICROPHONE METHOD INSTRUMENTATION

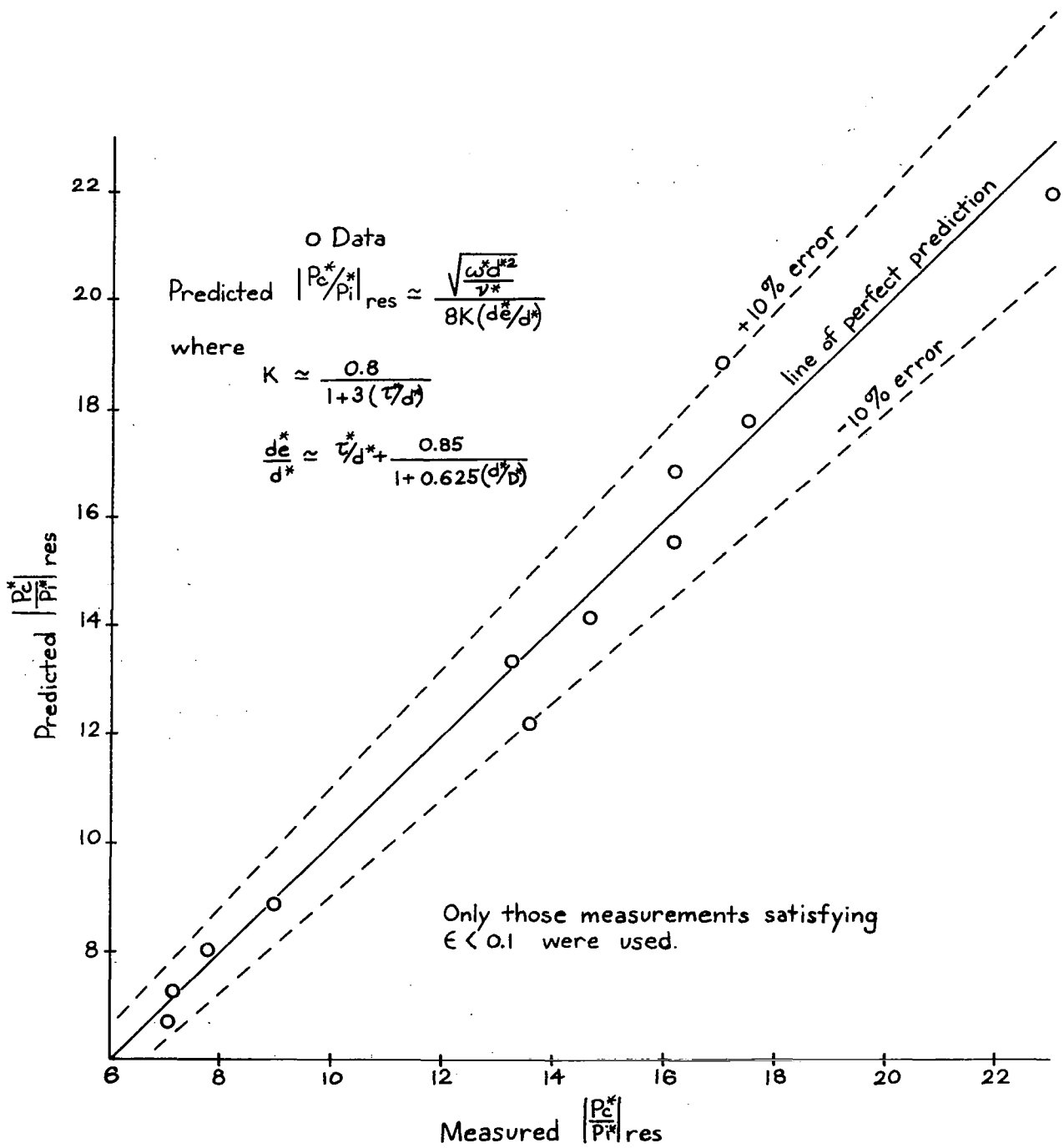


FIGURE 4. COMPARISON BETWEEN PREDICTED AND MEASURED CAVITY-TO-INCIDENT SOUND PRESSURE AMPLITUDE RATIO AT RESONANCE IN THE LOW SPL RANGE

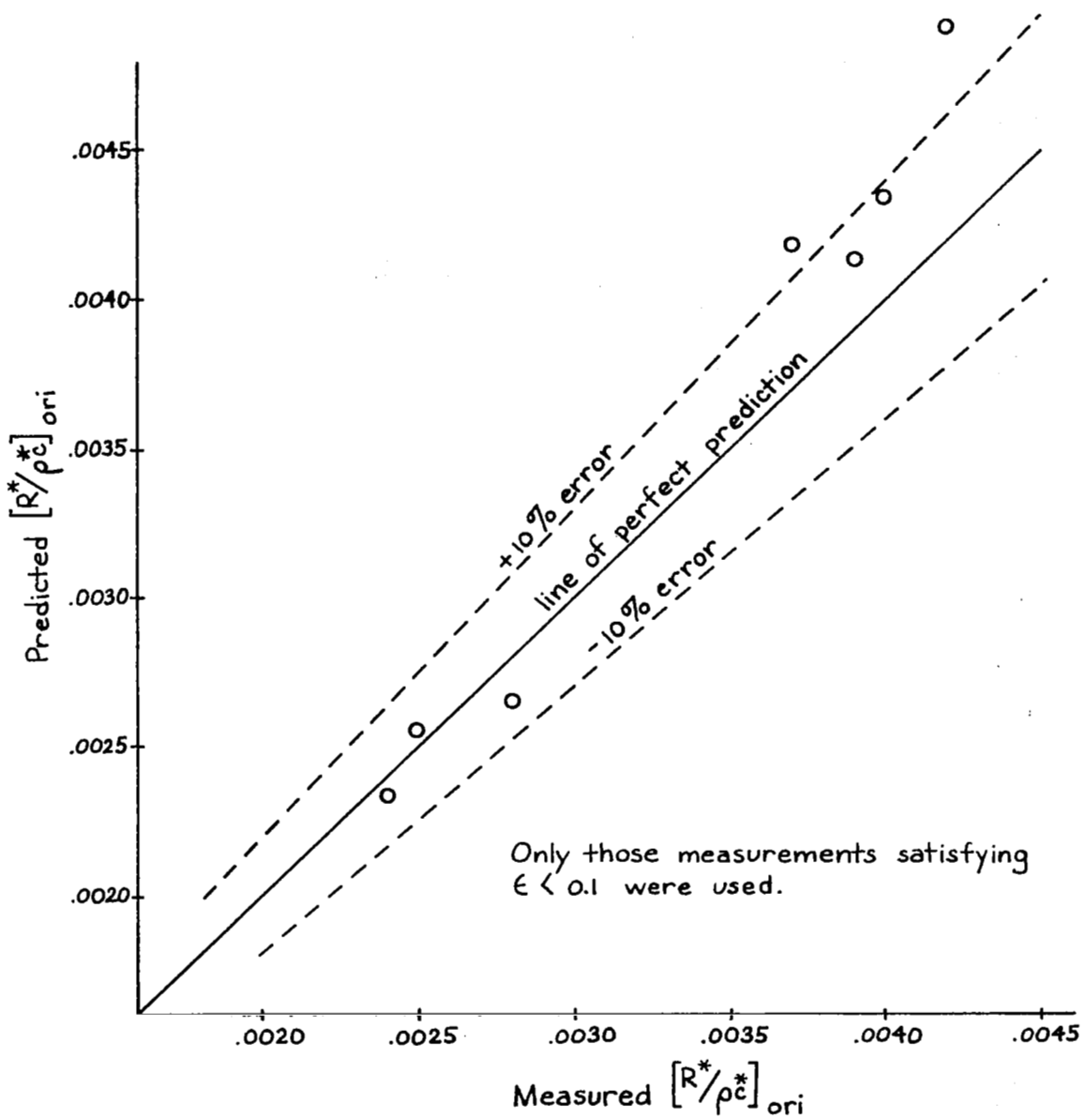


FIGURE 5. COMPARISON BETWEEN PREDICTED AND MEASURED RESONATOR RESISTANCE AT RESONANCE IN THE LOW SPL RANGE

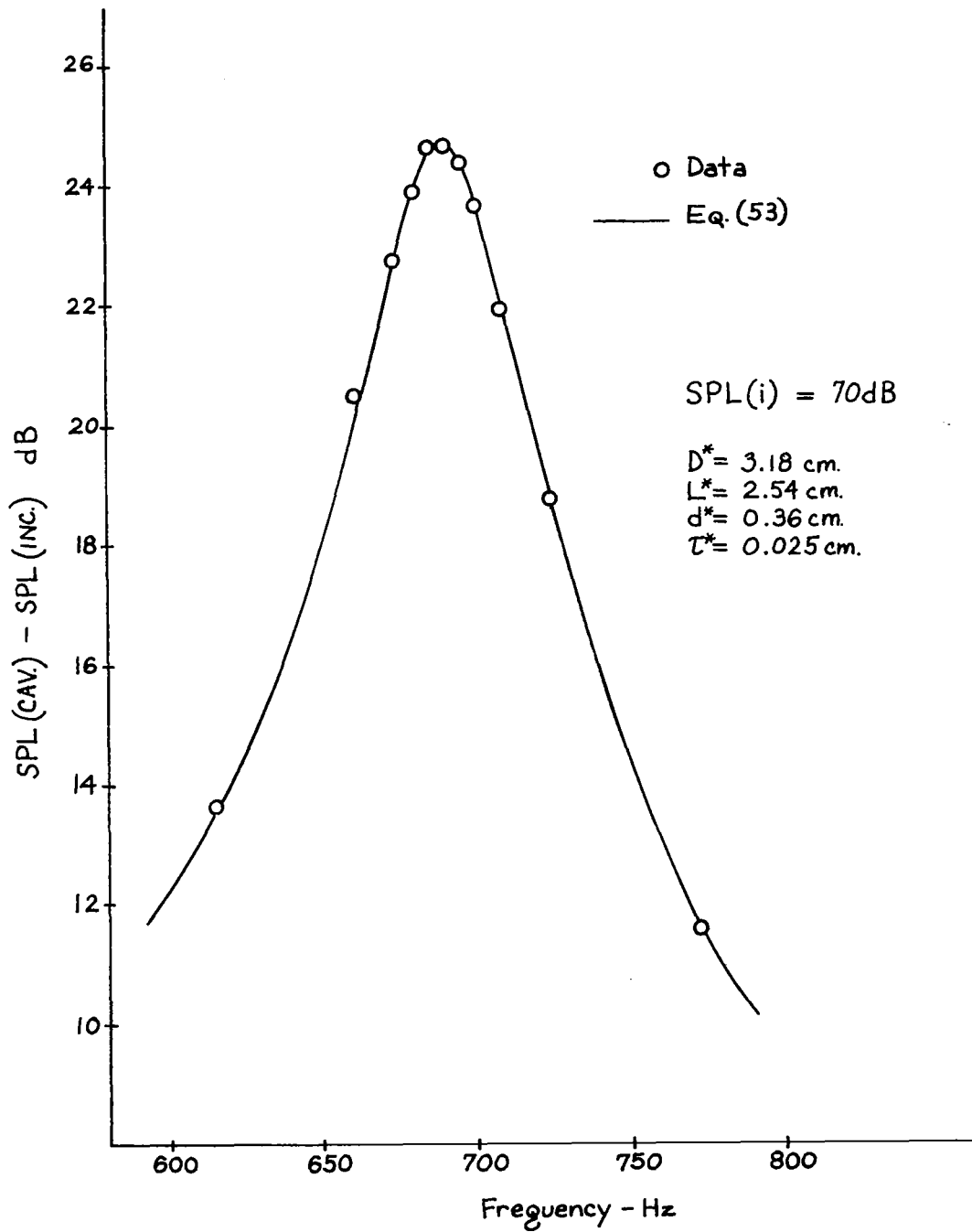


FIGURE 6. COMPARISON BETWEEN PREDICTED AND MEASURED CAVITY-TO-INCIDENT SOUND PRESSURE LEVEL CHANGE IN THE LOW SPL RANGE

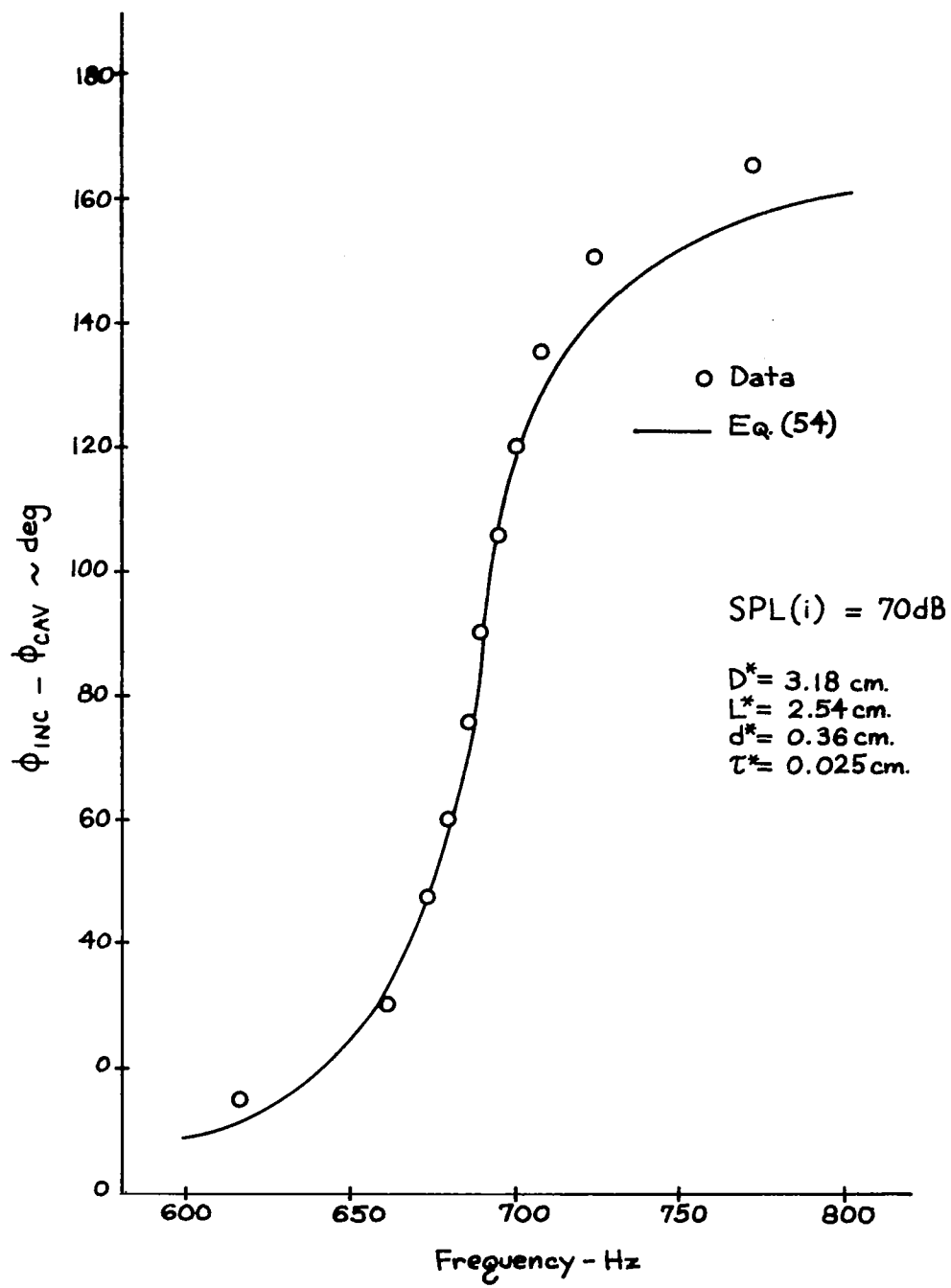


FIGURE 7. COMPARISON BETWEEN PREDICTED AND MEASURED PHASE CHANGE IN THE LOW SPL RANGE

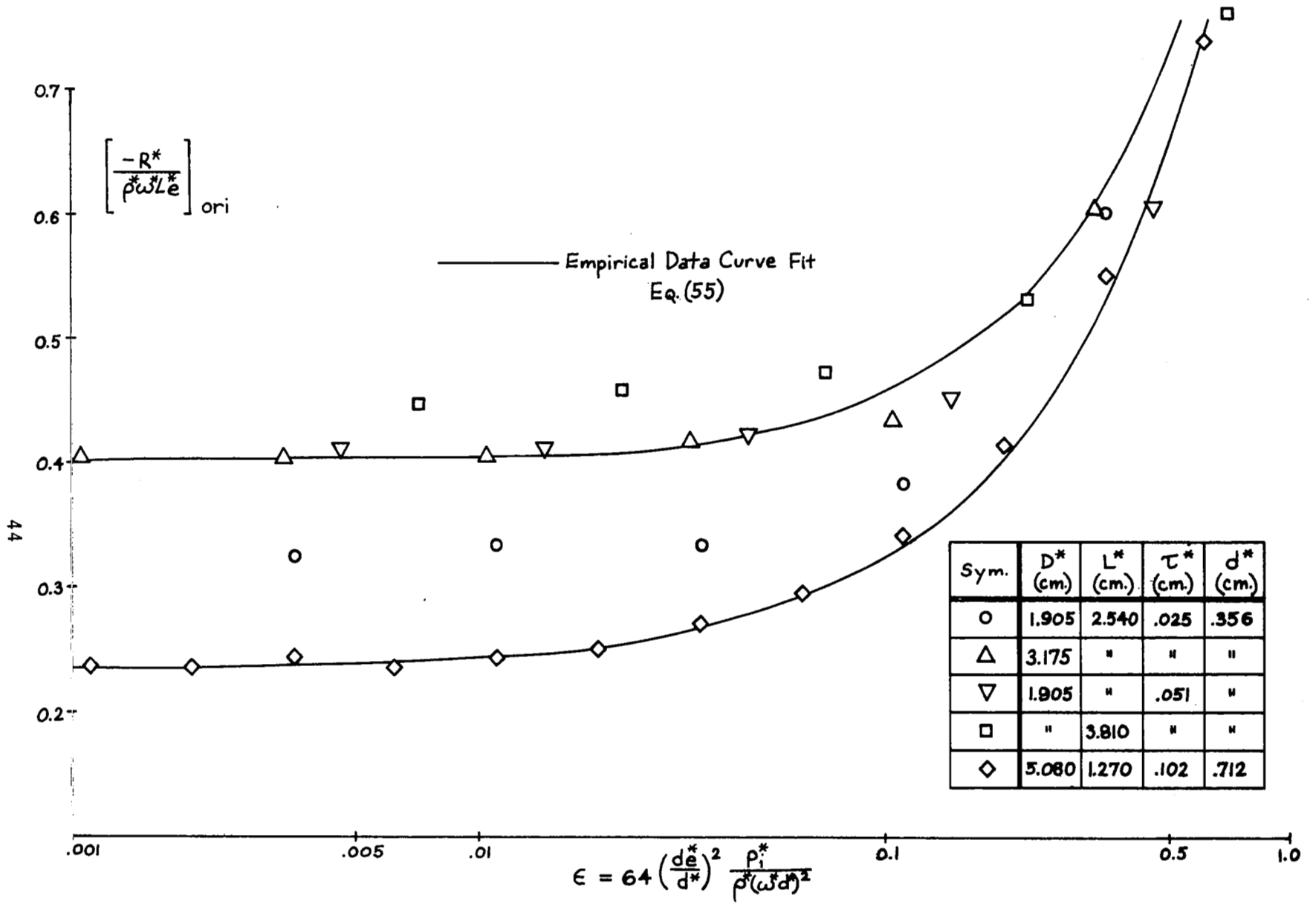


FIGURE 8. COMPARISON BETWEEN PREDICTED AND MEASURED WEAKLY NONLINEAR RESONATOR RESISTANCE

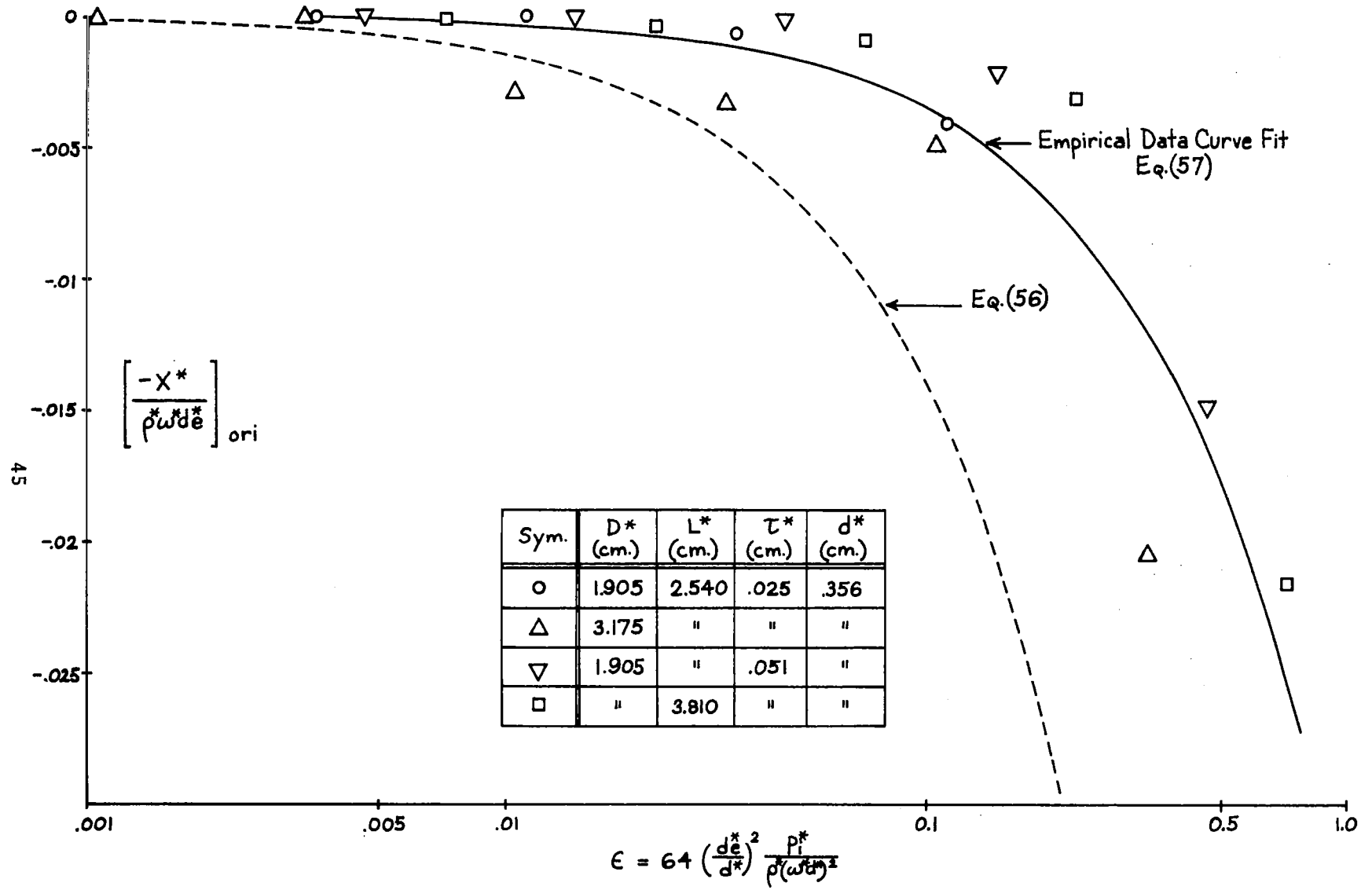


FIGURE 9. COMPARISON BETWEEN PREDICTED AND MEASURED WEAKLY NONLINEAR RESONATOR REACTANCE

Sym.	D* (cm.)	L* (cm.)	τ^* (cm.)	d* (cm.)
○	1.905	2.54	.051	.091
△	"	3.810	"	"
◇	"	"	.102	"
□	"	"	.051	.178
▽	3.175	"	.102	"

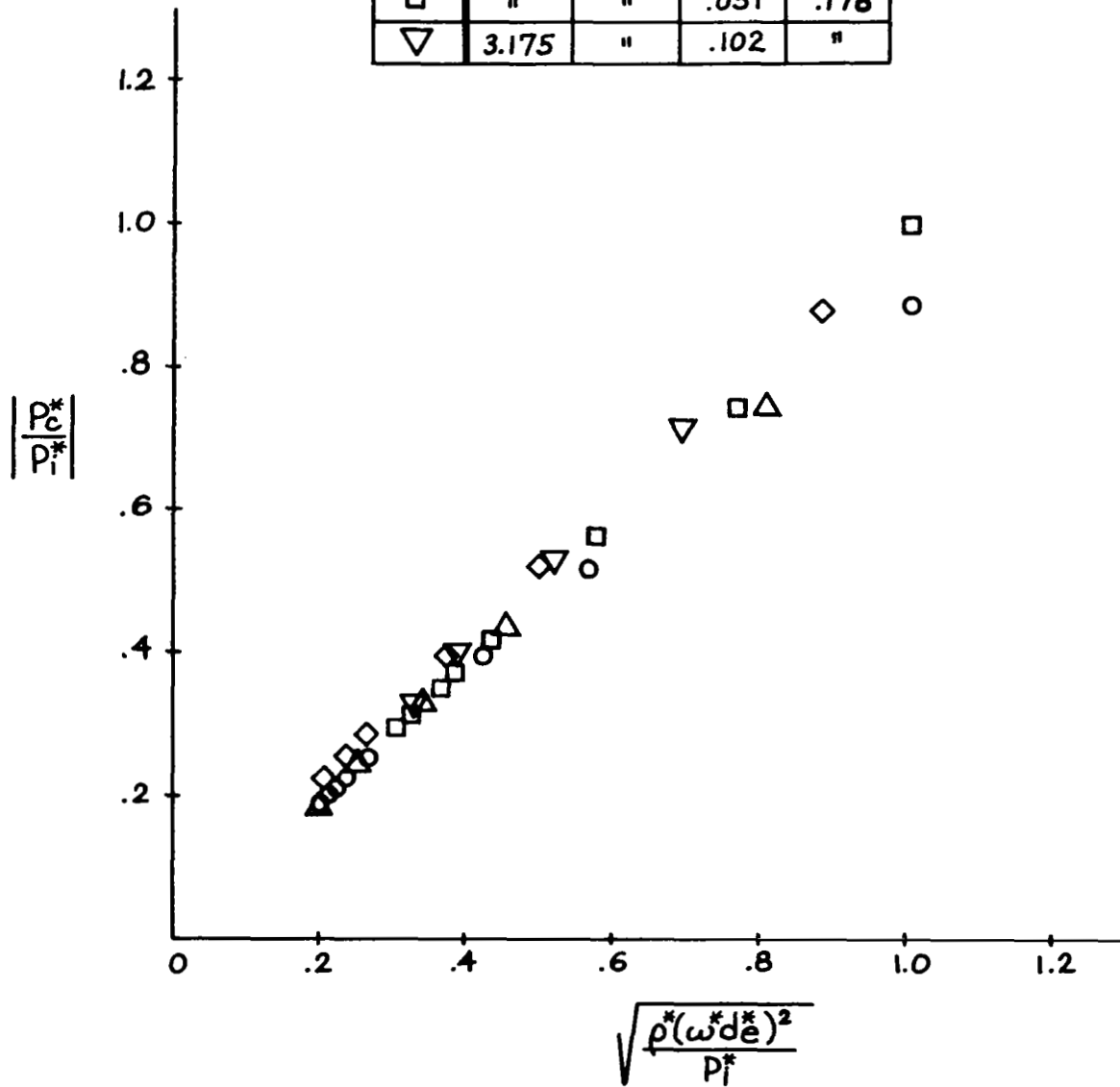


FIGURE 10. NONLINEAR RESPONSE OF CAVITY SOUND FIELD AT RESONANCE

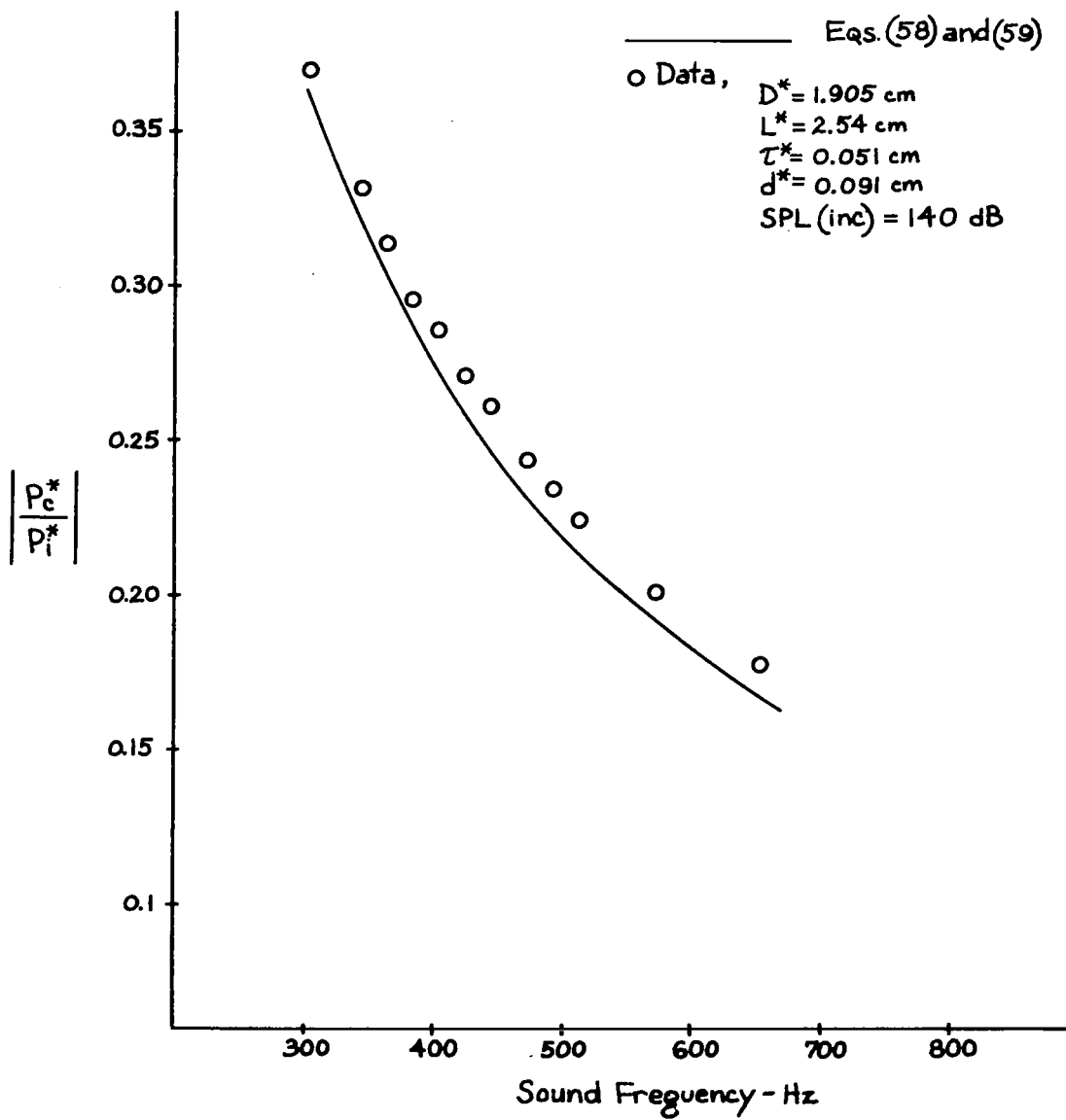


FIGURE 11. COMPARISON BETWEEN PREDICTED AND MEASURED $\left| \frac{P_c^*}{P_i^*} \right|$ VARIATION WITH FREQUENCY IN THE HIGH SPL RANGE

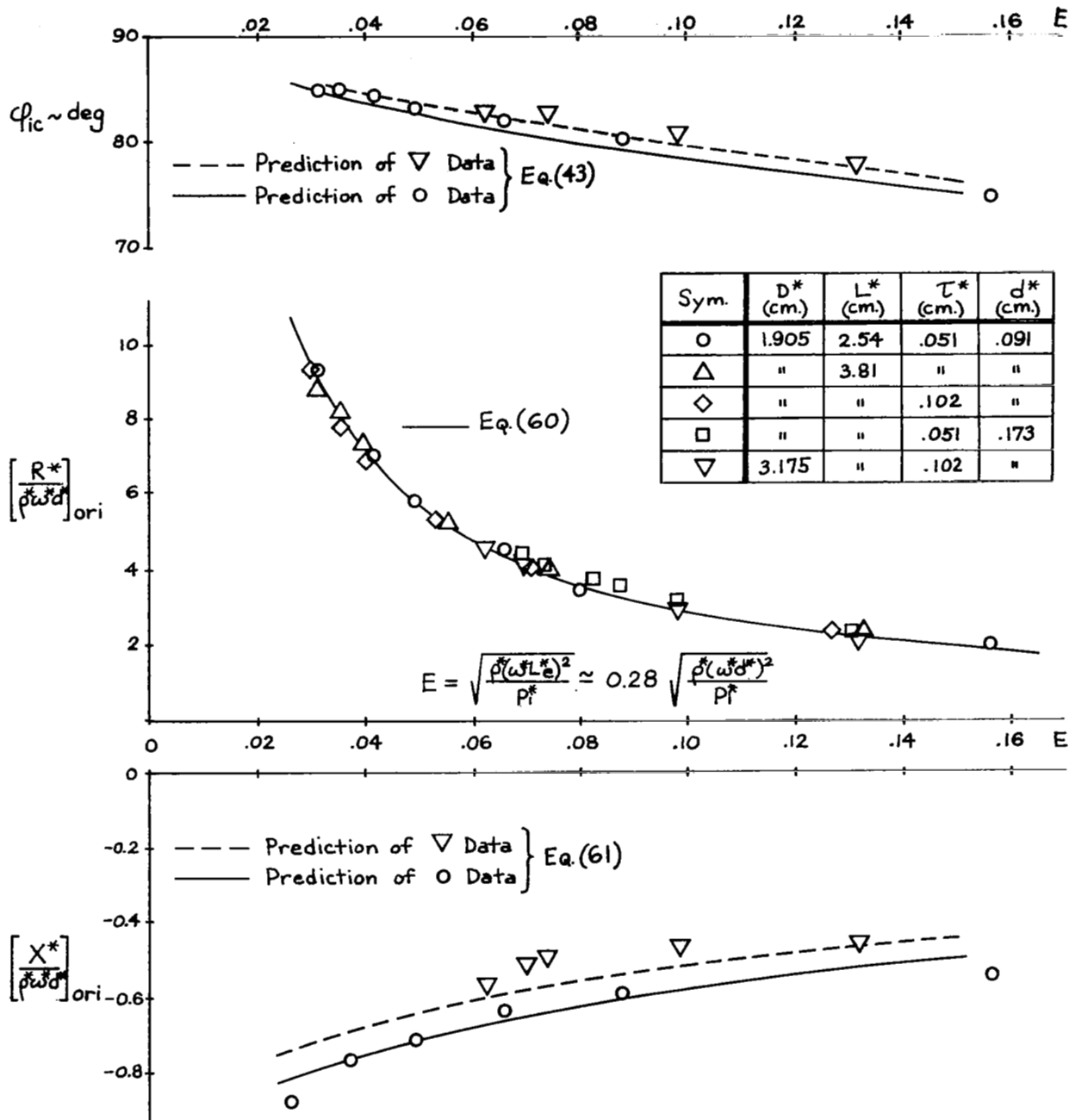


FIGURE 12. COMPARISON BETWEEN PREDICTED AND MEASURED RESONATOR BEHAVIOR AT RESONANCE IN THE NONLINEAR SPL RANGE

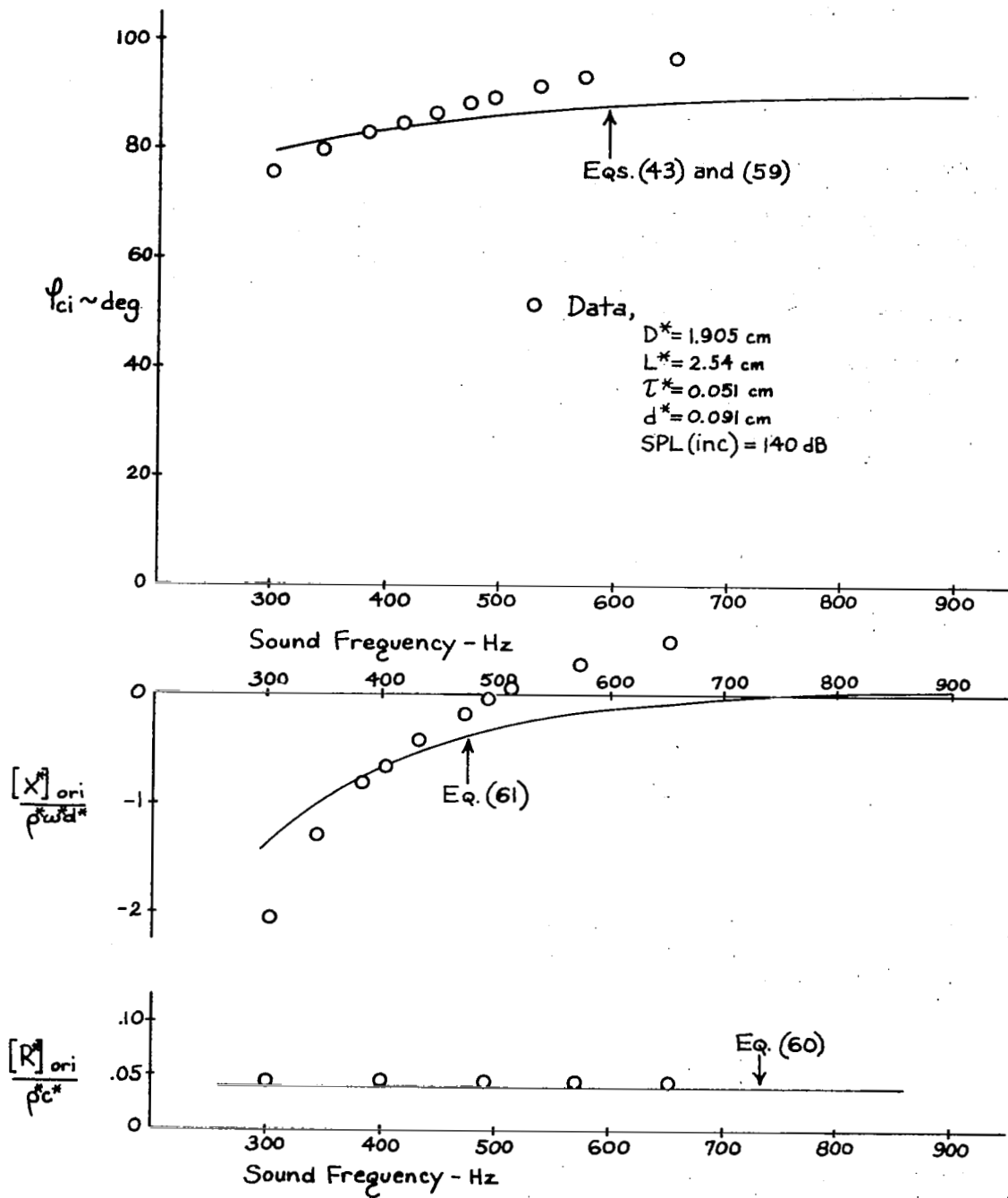


FIGURE 13. COMPARISON BETWEEN PREDICTED AND MEASURED RESONATOR FREQUENCY RESPONSE IN THE HIGH SPL RANGE

APPENDIX A

DERIVATION OF NONLINEAR FOURIER COEFFICIENTS

A detailed derivation of Eq. (42) and the subsequent calculation of the fundamental Fourier coefficients a_1 and b_1 follow.

The derivation starts from Eq. (39a). Recall from the discussion following Eq. (39a) that expansion of the function $G(t;E)$ in a regular power series of E leads to the approximate solutions $G_0(t)$ and $G_1(t)$ defined by Eq. (41). These solutions become singular at $t=(2n-1)\pi/2$. An approximate solution to $G(t;E)$ is derived below *valid throughout the half-cycle* $(4n-1)\pi/2 < t < (4n+1)\pi/2$ (hereafter $n=0$ without loss of generality).

The derivation proceeds as follows. The half-cycle $-\pi/2 < t < \pi/2$ is divided into the six regions shown in Fig. A-1. Region 1 is defined by the interval $0 < t < \pi/4$, Region 2 by $\pi/4 < t < T$ where T will be specified later and Region 3 by $T < t < \pi/2$. Regions -1, -2 and -3 are defined by the intervals $-\pi/4 < t < 0$, $-T < t < \pi/4$, and $-\pi/2 < t < -T$ respectively.

It will prove convenient to rescale Eq. (39a) by introducing the following transformations,

$$G(t;E) = \sqrt{2} g(t; s) ; \quad s = \sqrt{2} E \quad (\text{A-1})$$

resulting in

$$2 g \dot{g} + s \left[\ddot{g} + \left(\frac{2\pi L e^* c^{*2}}{V^* \omega^{*2}} \right) g \right] = -\sin(t) \quad (\text{A-2})$$

The absolute value operator $|(\)|$ is removed because only particle inflow ($g > 0$) is considered. Since the independent variable t is unaffected by the above transformation, the regions defined in Fig. A-1 still apply. An approximate solution to Eq. (A-2) is derived valid in Regions 1 and -1 by expanding $g(t;s)$ as follows,

$$g(t; s) \approx g_0(t) + s g_1(t) + \dots \quad (\text{A-3})$$

Substituting Eq. (A-3) into Eq. (A-2) and collecting coefficients of the first two powers of s yields

$$2 g_0 \dot{g}_0 = -\sin(t) \quad \text{and} \quad 2 g_0 \dot{g}_1 + 2 \dot{g}_0 g_1 = -\ddot{g}_0 - \left(\frac{2\pi L e^* c^{*2}}{V^* \omega^{*2}} \right) g_0 \quad (\text{A-4})$$

Approximate solutions to Eq. (A-4) are

$$g_0(t) = \sqrt{\cos(t)}; \quad g_1(t) \approx \frac{1}{4} \tan(t) - \left(\frac{2\pi L_e^* c^{*2}}{V^* \omega^{*2}} \right) \left(\frac{t}{2} + \frac{t^3}{12} \right) \quad (\text{A-5})$$

In deriving $g_1(t)$, the function $g_0(t)$ was approximated by $(1-t^2/4)$. This approximation restricts the solution $g_1(t)$ to Regions 1 and -1.

To derive approximate solutions valid in Region 2, Eq. (A-2) is transformed as follows,

$$g(\tau; s) = g(t; s); \quad \tau = \frac{\pi}{2} - t \quad (\text{A-6})$$

Under these transformations, Eq. (A-2) becomes

$$s \left[\frac{d^2 g}{d\tau^2} + \left(\frac{2\pi L_e^* c^{*2}}{V^* \omega^{*2}} \right) g \right] - g \frac{dg}{d\tau} = -\cos(t) \quad (\text{A-7})$$

Expanding $g(\tau; s)$ in a regular perturbation power series of s ,

$$g(\tau; s) \approx g_0(\tau) + s g_1(\tau) + o(s^2) \quad (\text{A-8})$$

and substituting into Eq. (A-7) yields the following approximate solutions

$$g_0(\tau) = \sqrt{\sin(\tau)}; \quad g_1(\tau) \approx \frac{1}{4} \cot(\tau) + \left(\frac{2\pi L_e^* c^{*2}}{V^* \omega^{*2}} \right) \left[\left(\frac{\tau}{3} + \frac{\tau}{63} \right) + \frac{A}{\sqrt{\tau}} \left(1 + \frac{\tau^2}{12} \right) \right] \quad (\text{A-9})$$

In the derivation of $g_1(\tau)$, $g_0(\tau)$ was approximated by $\sqrt{\tau}(1-\tau^2/12)$. Here A is a constant of integration. To match the solutions $g_0(t) + s g_1(t)$ at $t=\pi/4$ to $g_0(\tau) + s g_1(\tau)$ at $\tau=\pi/4$, the interface between Regions 1 and 2, the constant $A \approx -0.59$.

Observe that Eq. (A-9) is singular at $\tau=0$ (or $t=\pi/2$). It is important to understand that the singularity occurs because the power series expansion used in its derivation (see Eq. A-8) assumes that *throughout the cycle*

$$\left| s \left[\ddot{g} + \left(\frac{2\pi L_e^* c^{*2}}{V^* \omega^{*2}} \right) g \right] \right| \ll \left| g \dot{g} \right| \quad (\text{A-10})$$

It is easy to show that the perturbation expansion given by Eq. (A-8) generates approximate solutions that violate Eq. (A-10). Consider the solution described by Eq. (A-9). Assuming that both τ and s are small, $g(\tau;s) \approx g_0(\tau) \approx \sqrt{\tau}$, which upon substituting into Eq. (A-10) and retaining only important terms yields the following inequality

$$\frac{s}{2\tau^{3/2}} \ll 1$$

Obviously, this is not satisfied for τ sufficiently small. The failure of the regular perturbation expansion described by Eq. (A-8) to satisfy the inequality described by Eq. (A-10) is manifested by the appearance of the singularities in Eq. (A-9). The method of singular perturbation theory is used to derive an approximate solution valid in Region 3. The singularities are removed by appropriate rescaling of the dependent and independent variables so that in Region 3 the terms on the LHS of Eq. (A-10) are of the same order as the nonlinear term on the RHS. To accomplish this, the following transformations are introduced

$$g(\tau, s) = s^m Y(\eta); \quad \eta = \frac{\tau}{s^n} \quad (\text{A-11})$$

Substituting these quantities into Eq. (A-7) yields

$$\begin{aligned} -s^{2m-n} 2Y \frac{dY}{d\eta} + s \left[s^{m-2n} \frac{d^2Y}{d\eta^2} + \left(\frac{2\pi L_e^* c^{*2}}{V^* \omega^{*2}} \right) s^m Y \right] \\ = -\cos(s^n \eta) \approx -1 + s^{2n} \frac{\eta^2}{2} \end{aligned} \quad (\text{A-12})$$

Since Region 3 is near $\tau=0$ (or $t=\pi/2$) it is reasonable to assume that the two highest derivatives are of equal order. This occurs when

$$2m - n = 1 + m - 2n \longrightarrow m = 1 - n$$

Replacing m by $1-n$ in Eq. (A-12) yields, after some rearrangement,

$$s^{2-3n} \left[\frac{d^2Y}{d\eta^2} - 2Y \frac{dY}{d\eta} \right] + \left(\frac{2\pi L_e^* c^{*2}}{V^* \omega^{*2}} \right) s^{2-n} \approx -1 + s^{2n} \frac{\eta^2}{2} \quad (\text{A-13})$$

Matching the leading terms on both sides

$$2-3n=0 \rightarrow n = 2/3, m = 1/3$$

Thus the appropriate equation governing the behavior of the particle velocity near $\tau=0$ (Region 3 in Fig. A-1) is

$$\frac{d^2 Y}{d\eta^2} - 2Y \frac{dY}{d\eta} + s^{4/3} \left(\frac{2\pi L_e^* c^{*2}}{V^* \omega^{*2}} \right) Y = -1 + s^{4/3} \frac{\eta^2}{2} + O(s^{8/3}) \quad (\text{A-14})$$

where from Eq. (A-11),

$$g(\tau; s) = s^{1/3} Y(\eta; s); \eta = \frac{\tau}{s^{2/3}} \quad (\text{A-15})$$

The quantity T in Fig. A-1 is identified by appropriate matching of the solution in Region 2 to the solution of Eq. (A-14). As a guide to the solution of Eq. (A-14), Eq. (A-9) is written, for τ small,

$$g(\tau; s) \approx g_0(\tau) + s g_1(\tau) \approx \sqrt{\tau} \left(1 - \frac{1}{12} \tau^2 \right) + s \left[\frac{1}{4\tau} - \frac{0.59}{\sqrt{\tau}} \left(\frac{2\pi L_e^* c^{*2}}{V^* \omega^{*2}} \right) \right]$$

Using Eq. (A-15) to replace τ by η and collecting coefficients of the various fractional powers of s ,

$$g(\eta; s) \approx s^{1/3} \left[\sqrt{\eta} + \frac{1}{4\eta} - \frac{5}{32\eta^{3/2}} \right] - 1.18 \left(\frac{2\pi L_e^* c^{*2}}{V^* \omega^{*2}} \right) s^{2/3} \left[\frac{1}{2\sqrt{\eta}} - \frac{1}{4\eta^2} + \frac{25}{64\eta^{3/2}} \right] + O(s^{5/3}) \quad (\text{A-16})$$

Comparing Eq. (A-16) to Eq. (A-15) suggests the following expansion for $Y(\eta; s)$ for proper matching,

$$Y(\eta; s) \approx Y_0(\eta) + s^{1/3} Y_1(\eta) + s^{2/3} Y_2(\eta) + \dots \quad (\text{A-17})$$

Substituting Eq. (A-17) into Eq. (A-14), and collecting the coefficients of the first two powers of s yields

$$\frac{d^2 Y_0}{d\eta^2} - 2 Y_0 \frac{dY_0}{d\eta} = -1 \quad (\text{A-18})$$

$$\frac{d^2 Y_i}{d^2 \eta^2} - 2 \frac{d}{d\eta} (Y_0 Y_i) = 0 \quad (\text{A-19})$$

Integrating with respect to η ,

$$\frac{d Y_0}{d \eta} - Y_0^2 = -\eta + A_0 \quad (\text{A-20})$$

$$\frac{d Y_i}{d \eta} - 2 Y_0 Y_i = A_1 \quad (\text{A-21})$$

where $()' \equiv d/d\eta()$ and A_0 and A_1 are constants of integration. The solution of Eq. (A-20) can be expressed in terms of the Airy function $A_i(\eta)$ as

$$Y_0(\eta) = -\frac{dA_i(\eta)}{d\eta} / A_i(\eta)$$

providing the constant $A_0=0$. A graph of its behavior is shown in Fig. A-2. The asymptotic behavior of $Y_0(\eta)$ can be shown (see Chapter 10 of the Handbook of Mathematical Functions published by NBS) to be

$$\text{Limit}_{\eta \rightarrow \infty} Y_0(\eta) = \sqrt{\eta} + \frac{1}{4\eta} - \frac{5}{32\eta^{5/2}} + o(\eta^{-4}) \quad (\text{A-22})$$

With $Y_0(\eta)$ known, Eq. (A-21) can be solved numerically to determine $Y_1(\eta)$. A plot of $Y_1(\eta)$ is shown in Fig. A-3. Its asymptotic behavior follows immediately upon substitution of Eq. (A-22) into Eq. (A-21) to yield,

$$\text{Limit}_{\eta \rightarrow \infty} Y_1(\eta) = -A_1 \left[\frac{1}{2\sqrt{\eta}} - \frac{1}{4\eta^2} + \frac{25}{64\eta^{5/2}} \right] + o(\eta^{-5}) \quad (\text{A-23})$$

The method of singular perturbation theory requires that the asymptotic behavior of the Region 3 function $Y(\eta;s)$ merge smoothly into the Region 2 function $g(\tau;s)$. Although mathematically, the matching occurs asymptotically, that is in the limit as $\eta \rightarrow \infty$, numerically, matching occurs for finite values (often less than 5) of the independent variable. Combining Eqs. (A-15), (A-17), (A-22) and (A-23) yields the following asymptotic behavior for the Region 3 functions,

$$\lim_{\eta \rightarrow \infty} g(\eta; s) = s^{1/3} \left[\sqrt{\eta} + \frac{1}{4\eta} - \frac{5}{32\eta^{5/2}} \right] - A_1 s^{2/3} \left[\frac{1}{2\sqrt{\eta}} + \frac{1}{4\eta} - \frac{25}{64\eta^{5/2}} \right] \quad (\text{A-24})$$

Comparing Eq. (A-24) above with Eq. (A-16) which represents the Region 2 solution written in terms of η , matching occurs providing the constant

$$A_1 = 1.18 \left(\frac{2\pi L_{ec}^* \omega^{*2}}{V^* \omega^{*2}} \right) \quad (\text{A-25})$$

The functions $Y_0(\eta)$ and $Y_1(\eta)$ are shown in Figures A-2 and A-3 respectively to be within one percent of their asymptotic behavior at $\eta=2$. This value of η is used to define Region 3. Substituting of $\eta=2$ in Eq. (A-15) yields $\tau=2s^{2/3}$. From Eq. (A-6) and Fig. A-1, this translates into $t=T \equiv \pi/2 - 2s^{2/3}$. Thus an approximate solution valid throughout $0 < \tau < \pi/2$ has been constructed. In a similar manner, approximate solutions can be constructed for Regions -1, -2, and -3. Foregoing the details, the various solutions are described below:

Region -1; $-\frac{\pi}{4} \leq t \leq 0$:

$$g(t; s) \approx g_0(\tau) + s g_1(\tau) \approx \sqrt{\cos(\tau)} - s \left[\frac{1}{4} \tan(t) - \left(\frac{2\pi L_{ec}^* \omega^{*2}}{V^* \omega^{*2}} \right) \left(\frac{t}{2} + \frac{t^3}{12} \right) \right] \quad (\text{A-26})$$

Region -2; $2E^{2/3} \leq \tau \leq \frac{\pi}{4}$ ($\tau = \frac{\pi}{2} + t$):

$$g(\tau; s) \approx g_0(\tau) + s g_1(\tau) \approx \sqrt{\tau} \left(1 - \frac{1}{12} \tau^2 \right) - s \left[\frac{1}{4\tau} - \frac{0.59}{\sqrt{\tau}} \left(\frac{2\pi L_{ec}^* \omega^{*2}}{V^* \omega^{*2}} \right) \right] \quad (\text{A-27})$$

Region -3; $0 \leq \eta \leq 2$; ($\eta = \tau/E^{2/3}$):

$$Y^-(\eta) \approx Y_0^-(\eta) + s^{1/3} Y_1^-(\eta) \quad (\text{A-28})$$

The notation Y^- denotes the function is valid in Region -3; the (Y^+) denotes Region 3. Graphs of the functions $Y_0(\eta)$ and $Y_1(\eta)$ are

shown in Figs. (A-2) and (A-3) respectively.

The above approximate solutions are valid throughout the half-cycle $-\pi/2 < t < \pi/2$. The corresponding fundamental harmonic coefficients a_1 and b_1 defined below as

$$a_1(E) = \frac{2}{\pi} \int_{-\pi/2}^{\pi/2} G(t; E) \cos(t) dt$$

$$b_1(E) = \frac{2}{\pi} \int_{-\pi/2}^{\pi/2} G(t; E) \sin(t) dt$$

are evaluated in the usual way. The results of the integration are

$$a_1(E) \approx 1.57 + 0.19 E^{5/3} + o(E^2) \quad (A-29)$$

$$b_1(E) \approx E \left[0.07 - 0.43 \ln(E) - \left(\frac{2\pi L e^* c^{*2}}{\sqrt{w^{*2}}} \right) (2.55 - 2.63 E^{1/3}) \right] \quad (A-30)$$

The major contribution to $a_1(E)$ comes from the regions $-\pi/4 \leq t \leq \pi/4$ while the major contribution to $b_1(E)$ comes from the regions $-\pi/2 \leq t \leq -\pi/4$ and $\pi/4 \leq t \leq \pi/2$.

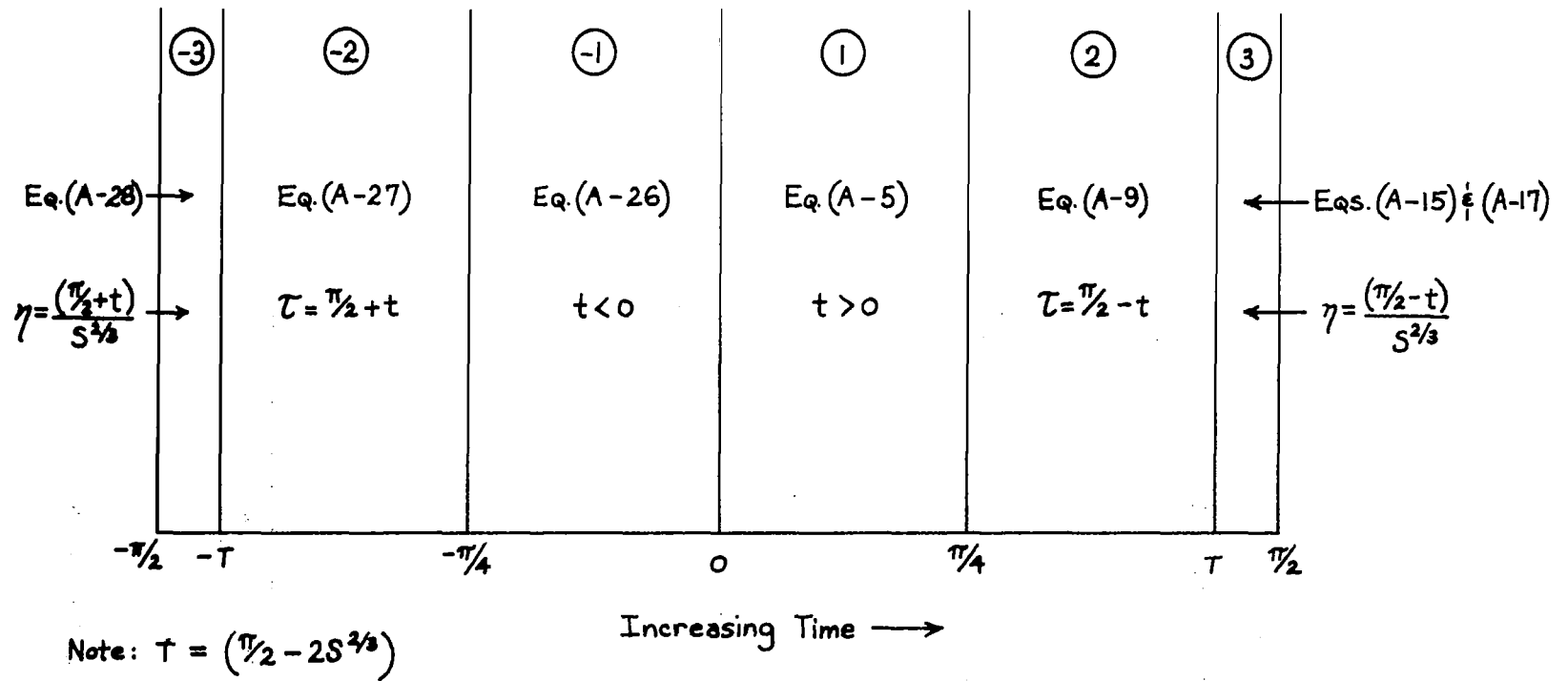


FIGURE A-1. DEFINITION OF HALF-CYCLE SUBREGIONS WITHIN WHICH INDICATED SOLUTIONS ARE VALID

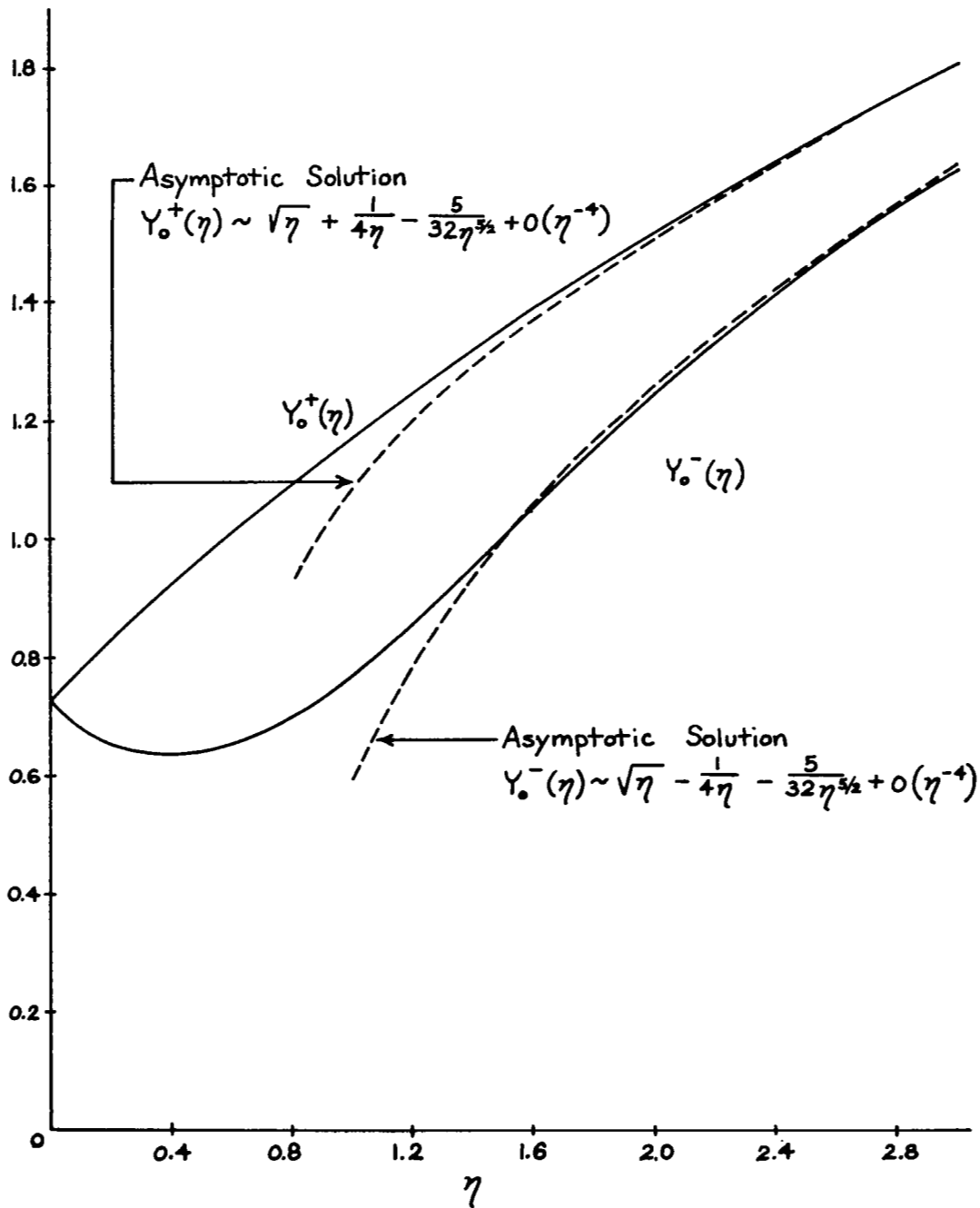


FIGURE A-2. DEFINITION OF THE FUNCTIONS $Y_0^+(\eta)$ and $Y_0^-(\eta)$

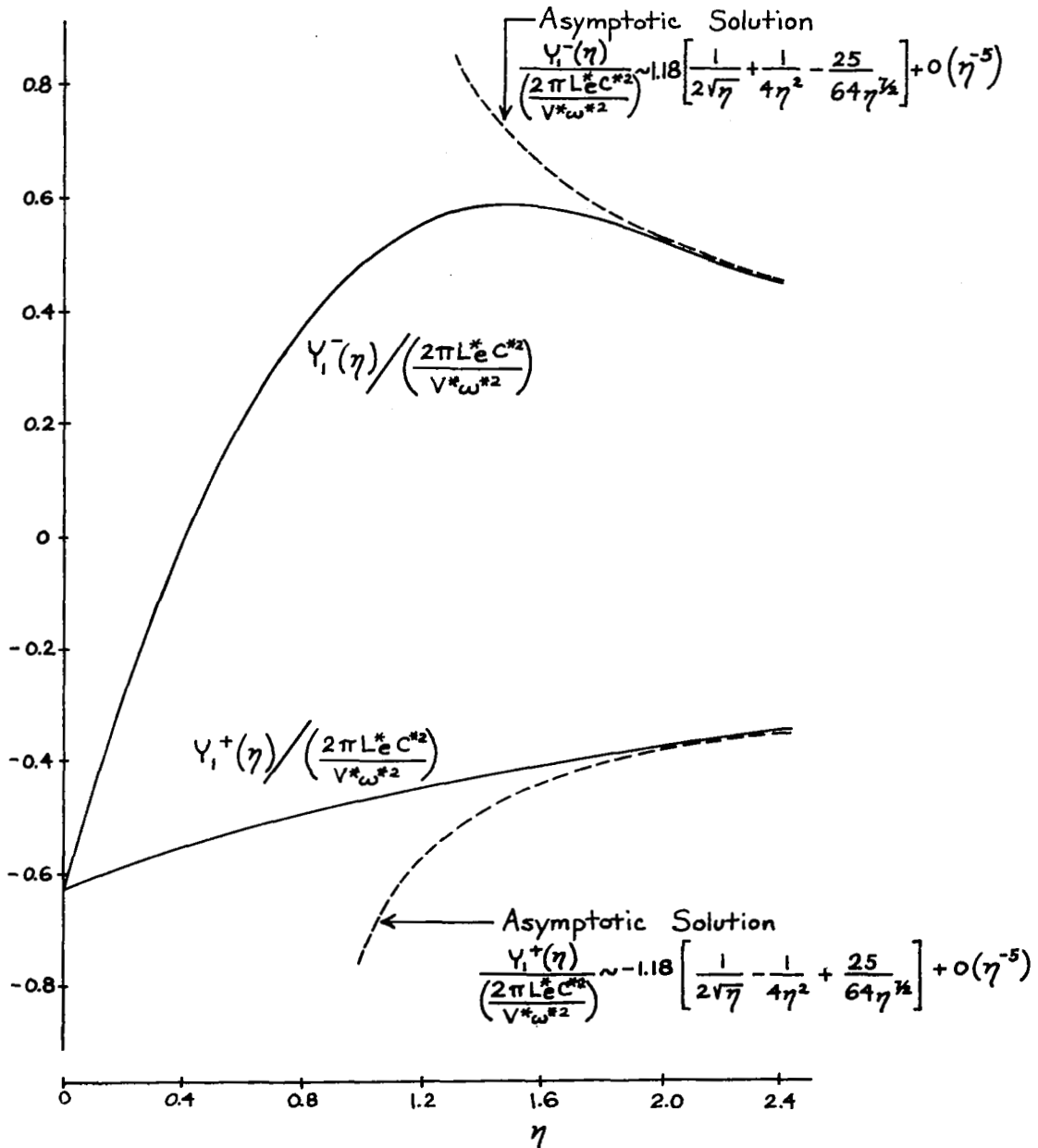


FIGURE A-3. DEFINITIONS OF THE FUNCTIONS $Y_1^+(\eta)$ and $Y_1^-(\eta)$

APPENDIX B

CORRECTION OF HIGH SPL DATA FOR THIN ORIFICE FACE PLATES

At very high incident sound pressure levels (150 dB and higher), the measured data showed that the very thin ($\tau^*=0.01$) orifice face sheets did not correlate well with the parameter E. This could be attributed to any, or possibly a combination of, three phenomena.

(1) Cross-modulation products of higher harmonics of the cavity sound field could combine with the transmitted fundamental signal, resulting in substantial phase shifts, even if the level of such cross modulation products were 20 dB or more below that of the fundamental. Quantitative evaluation of this effect would require knowledge of the amplitudes and phases of all the harmonics, as well as an understanding of the non-linear process which generates the cross modulation. Since at incident levels of 150-160 dB, where phase correlation is poorest, the incident field contains considerable 2nd harmonic distortion, there is probably some cross modulation occurring in the orifice as well as within the cavity, further compounding the difficulties.

(2) Due to the physical size of the microphones required for use at 70 dB incident level (1/2" diameter) it is necessary to mount the cavity microphone at the rear of the cavity. At low to moderate incident sound levels, the cavity microphone is expected to measure the response of the entire fluid contained within the cavity. At high sound pressure levels, however, the influx of fluid into the cavity is characterized by strong jetting. If the jet does not decay before reaching the microphone, a stagnation pressure velocity would result from the impingement of the jet on the microphone diaphragm, giving an altered phase angle and effective cavity sound pressure level. Observation of the cavity sound pressure signal on an oscilloscope at high incident level, reveals, for the larger values of d^*/L^* , an instability in the wave form on one half cycle, which we believe to be related to this phenomenon.

In an attempt to quantify this effect, a small hole was drilled into the side of one of the cavities, into which a 1/8" diameter microphone was inserted. The output from this microphone and that from the 1/2" microphone at the back of the cavity were observed simultaneously on the oscilloscope as the incident sound pressure level was increased from 90 to 155 dB. At the higher levels, the wave instability reappeared on the 1/2" microphone trace, but was absent from the 1/8" microphone trace. Although the general wave shape of the two microphone signals was similar and there appeared to be a slight advance in phase of the 1/2" microphone signal with increasing incident sound pressure level, the phase and amplitude of the 1/8" microphone signal was judged too unreliable to make conclusive judgements since it was extremely sensitive to slight changes in position.

(3) It was observed that the cavities with small values of τ^* and L^* exhibited the poorest phase correlation. This suggested that the face plate of the cavity was being flexed by the incident sound pressure, effectively modulating the volume of the cavity and hence increasing the cavity pressure in phase with the incident pressure. This would have the effect of both advancing the phase of the cavity sound field and increasing the cavity sound pressure level.

As a test of this possibility, the case that exhibited the poorest correlation, ($D^* = 1.25''$, $L^* = 0.5''$, $d^* = .036''$ and $\tau^* = .010$) was remeasured with the orifice covered. At low incident levels, the face plate flexure was inconsequential. However, at 150 dB, it resulted in a phase advance of 28 degrees and a cavity pressure increase of 1.5 dB.

These results were sufficiently encouraging that several of the other samples which had given poor phase correlations were re-measured using this technique. In each case the phase correlation was improved, but the degree of improvement depended upon the face plate thickness and cavity dimensions. Results of the most significantly improved cases are plotted in Figure B-1 for phase.

The better improvement in phase correlation achieved with the thinner face plates and smaller orifice diameters suggests that Phenomena #2 & #3 are both affecting the phase, and to a lesser extent the amplitude of the cavity sound pressure. We believe that without properly accounting for pressure change on the face plate due to flow through the orifice, the plate flexing correction is excessive. For the case of the thin face plate, small d^*/D^* models, this excess is minimal because of low airflow due to the high orifice resistance. Hence the phase correlation has been improved for these models.

In order to obtain a better understanding of the jet impingement phenomenon, a resonator with the dimensions $D^* = .75''$, $L^* = .75''$, $d^* = .07''$, $\tau^* = .02''$ was tested with the standard 1/2" microphone at the back of the cavity and the 1/8" microphone at the side of the cavity. The outputs from these two microphone were fed to the AD-YU Phase meter and simultaneously observed on the dual trace oscilloscope. The measurement procedure was as follows. First, the frequency of the incident sound was tuned at a low level to the resonance frequency. The level was then increased until the onset of the wave instability (from the output from the 1/2" microphone signal) appeared on the oscilloscope. It was observed (see Fig. B-2) that the instability occurred in the trough of the oscilloscope wave at an incident level of 145 dB. As the level was increased, the instability moved forward on the wave, reaching the crest of the wave at 150 dB and starting down the leading edge when the system limitation for the particular drive frequency was reached at 153 dB. This suggests a sound pressure level dependent delay time for whatever is causing the instability at the microphone. The jet from the orifice is an obvious candidate, since it would travel from the orifice to the microphone at an average velocity related to the particle velocity

in the orifice.

To support the hypothesis that the jet impingement caused the nonlinear phase and amplitude shifts, the average jet travel time from the orifice to the cavity backing was measured and correlated with the particle velocity u in the orifice. Since the jet enters the cavity at the maximum (vena contracta) value of particle velocity, it would originate at a time corresponding to a positive-going zero crossing of the cavity pressure (negative going on the scope trace, since the condenser microphone by its nature inverts the signal). The delay of the instability by some fraction (possibly >1) of a wavelength on the trace could then be related to its travel time if we were able to identify the zero crossing associated with each instability. To identify this, the position in *time* of each instability was noted while the oscilloscope trace was started at the negative-going zero crossing. Holding the amplitude constant, the frequency was shifted downward 10%. As expected, the instabilities relative position on the wave changed; the position in time of only one instability remained constant, as illustrated by the two sketches shown in Figure B-3. One may conclude that the instability which stayed constant in time was due to the high particle velocity which occurred at the beginning of the oscilloscope trace, so by knowing the oscilloscope sweep speed, the mean travel time of the jet from the orifice to the microphone at the back of the cavity may be determined.

As an example, for the model checked, at an incident level of 151 dB, the delay of the jet arrival was found, from the oscilloscope, to be $3/4$ wavelength at 784 Hz, corresponding to a travel time of 0.96 millisecond. Since the cavity depth is 0.75" (or 0.019 meters), this corresponds to a mean jet velocity of 20 meters per second. The peak orifice velocity, in accordance with Eq. (44), would, at 151 dB, be 33.5 meters per second. This would indicate an average jet speed of 60% maximum, which is not unreasonable. If we estimate a linear deceleration in the cavity, this would result in a peak pressure level of 122.5 dB at the microphone, as opposed to a peak level of 147 dB for the uncontaminated wave, or approximately 19% contribution. From the appearance of the oscilloscope trace this seems to be a high estimate, demonstrating the approximate nature of the linear deceleration assumption.

The series of sketches in Figure B-3 shows how this level dependent travel time can contaminate the phase data from the two microphone method unless precautions are taken to prevent jet impingement on the cavity microphone. Note that there is (obviously) one jet instability per wave length, and that these would be expected to have the form of a somewhat unstable positive pressure pulse train, whose relative position on the cavity pressure wave depends on the mean travel time, and hence on the incident pressure, the cavity depth and the decay rate of the jet.

Since the composite signal is processed through a narrow band filter, only the Fourier component at the test frequency will affect the final results. This is displayed in Fig. B-3. It will be noted

that the relative phase of this signal will follow the relative position of the pulse train.

Figure B-4 shows the position of the pulses at three sound levels for the model tested at incident levels of 145, 148, 150 and 153 dB. Visual estimate of the amplitude of the jet pulse is approximately 3% of the total wave. If we estimate that the fundamental component is 1% of the total, the phase of the contaminated signal relative to the uncontaminated would be as shown in the following table, for the case illustrated in Figure B5.

SPL_{inc}	ΔSPL_{inc}	$\Delta\phi$	$\phi_C(\text{total})$
145	40dB	90°	.6°
148	40dB	30°	.3°
150	40dB	-60°	-.5°
153	40dB	-120°	-.5°

If the amplitude of the contaminating wave were actually 3% of the total, the phase angle error would be increased proportionately, and this fraction could be even higher for small cavity depths and large orifices.

One previously unexplained measurement inconsistency can now be at least qualitatively understood. In some of the cavities tested the phase was noted to approach 90° as the level was increased, and then, at very high levels, to decrease again, causing reactance from Dean's model to become much too negative to be physically meaningful. As shown earlier, this was attributable in part to face plate flexure and in part to jet impingement. However, it was observed that the phase would occasionally go past 90° at very high levels. This effect could not be explained by face plate flexing. However, we see now that if the level, frequency and orifice to microphone distance are present in the correct combination to allow the jets to arrive at the microphone during the negative half cycles of the cavity pressure, a positive phase perturbation results.

Conclusion

We now see that in order to obtain phase and reactance data with sufficient accuracy to test the theoretical model at high incident sound levels, some basic limiting characteristic of the two microphone method not previously considered in the literature will have to be either avoided or quantified.

The cavity flexure problem is probably not too important, since the very thin unsupported orifice plates for which it appears to be a dominant factor are probably not feasible for practical application. It is also a real effect which depends on the geometry of the test specimen rather than the measurement procedure.

The jet impingement and cross modulation phenomena, on the other hand, represent effects which are detected inside the cavity,

but which have no bearing on the true surface impedance of the cavity as seen from the incident sides. The cross modulation problem is unavoidable. The jet impingement problem might be avoided by changing the microphone location.

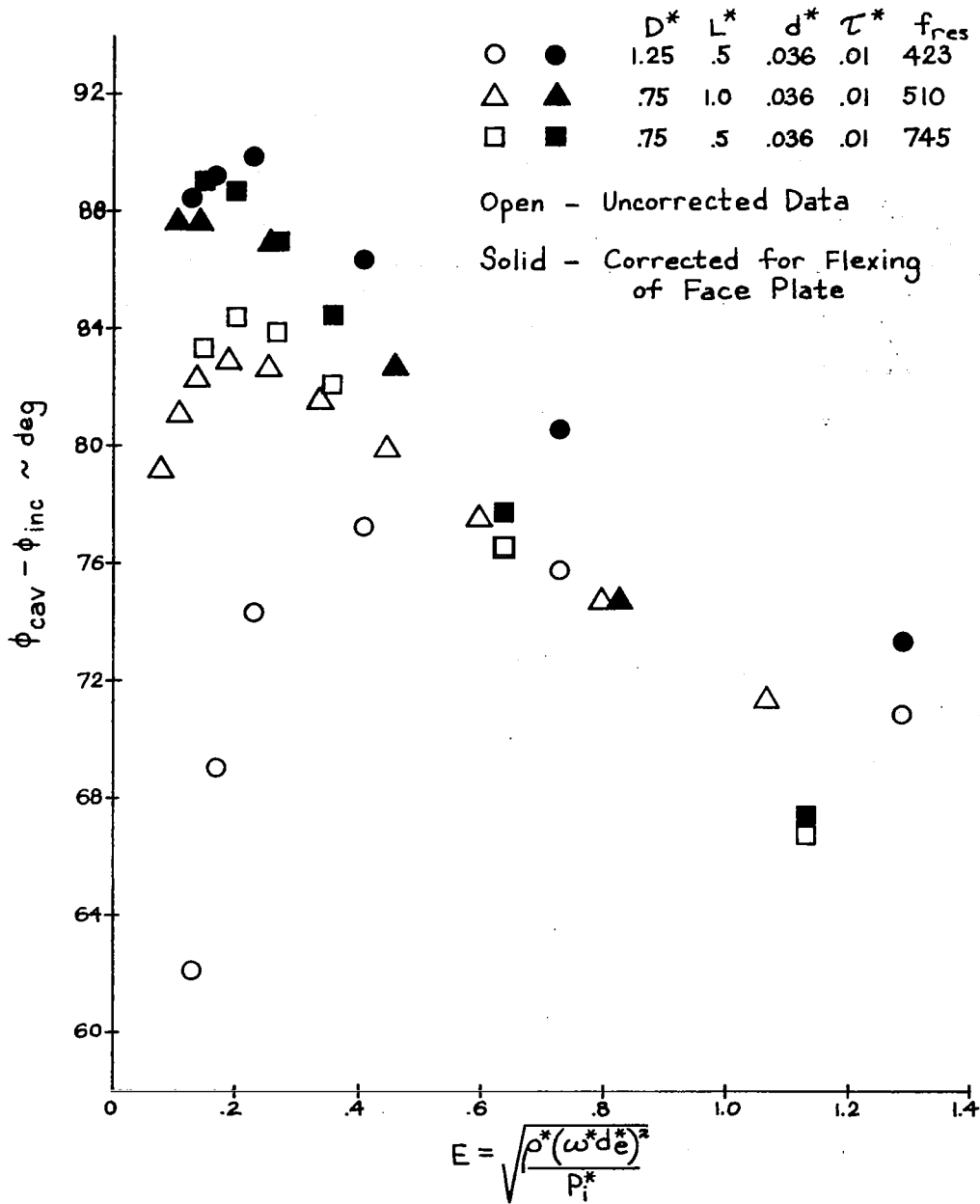
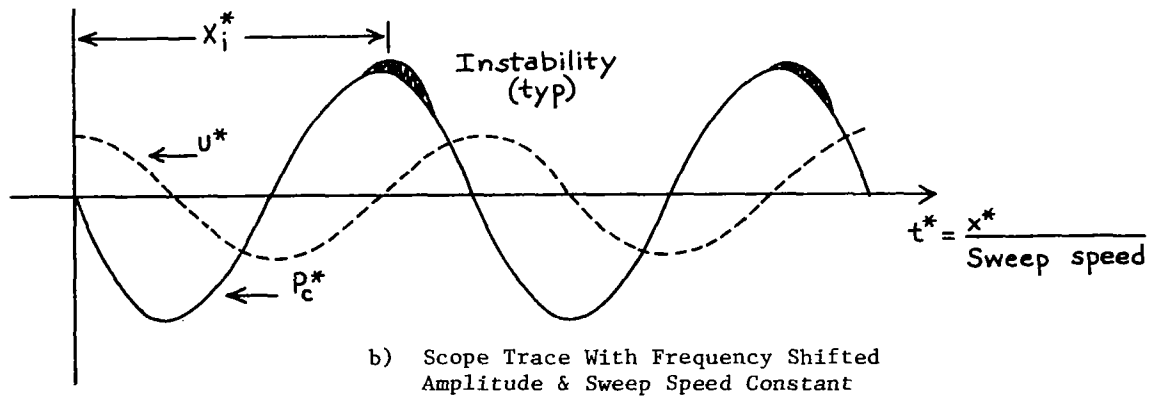
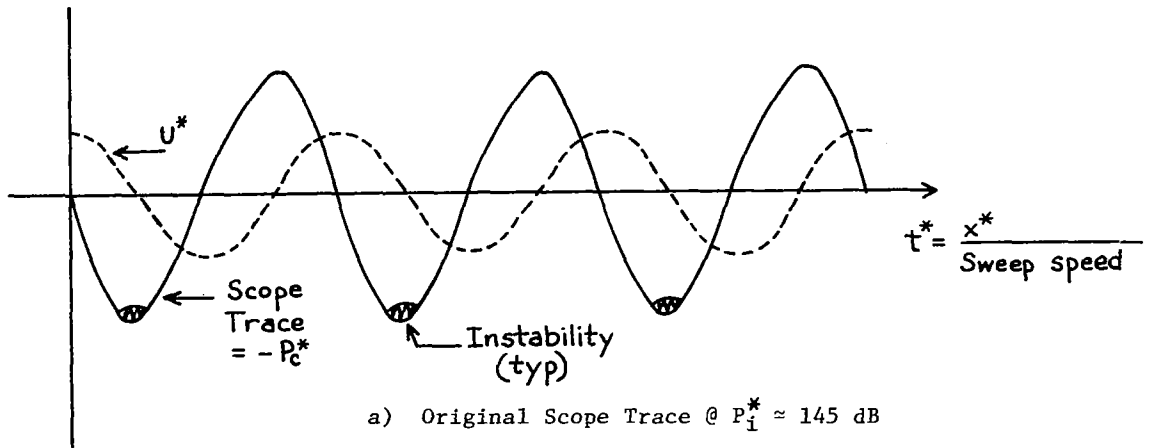
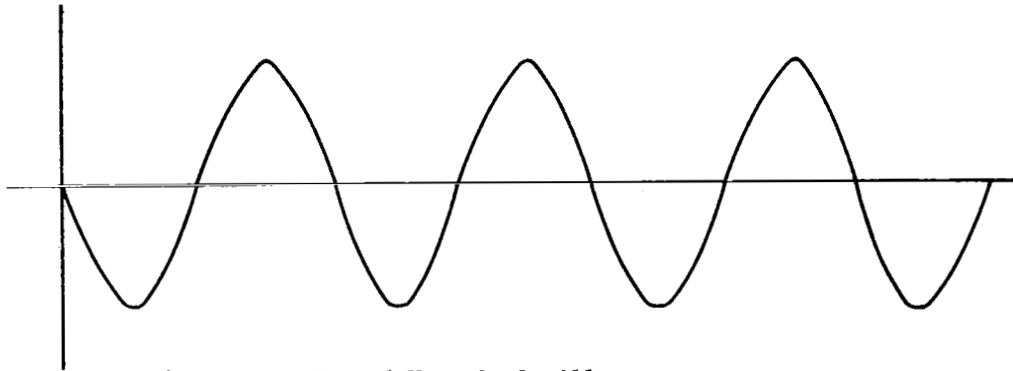


FIGURE B-1. COMPARISON BETWEEN PREDICTED AND MEASURED PHASE CHANGE ACROSS ORIFICE IN THE HIGH SPL RANGE

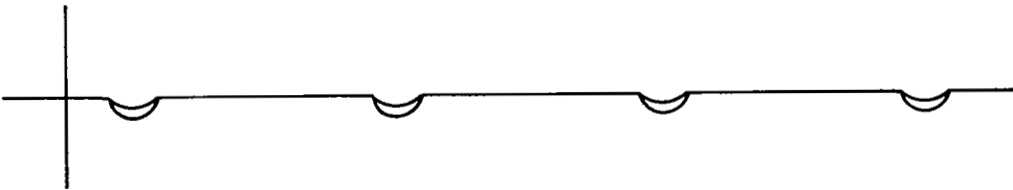


Mean Travel Time $\approx X_i^*/\text{Sweep Speed}$

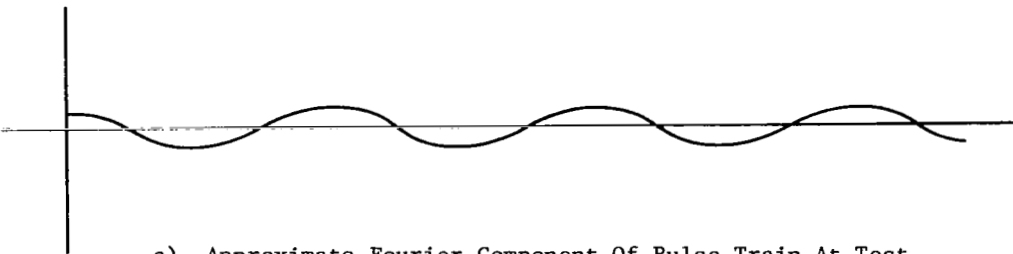
FIGURE B-2. DETERMINATION OF MEAN TRAVEL TIME OF JET



a) Uncontaminated Wave On Oscilloscope



b) Pulse Train Of Jet Arrivals; Moves To The Left
As Incident Level Is Increased



c) Approximate Fourier Component Of Pulse Train At Test
Frequency; Phase Advances As Incident Level Is Increased

FIGURE B-3. PHASE RELATIONSHIP OF FUNDAMENTAL FOURIER COMPONENT
OF JET PULSE TO UNCONTAMINATED WAVE

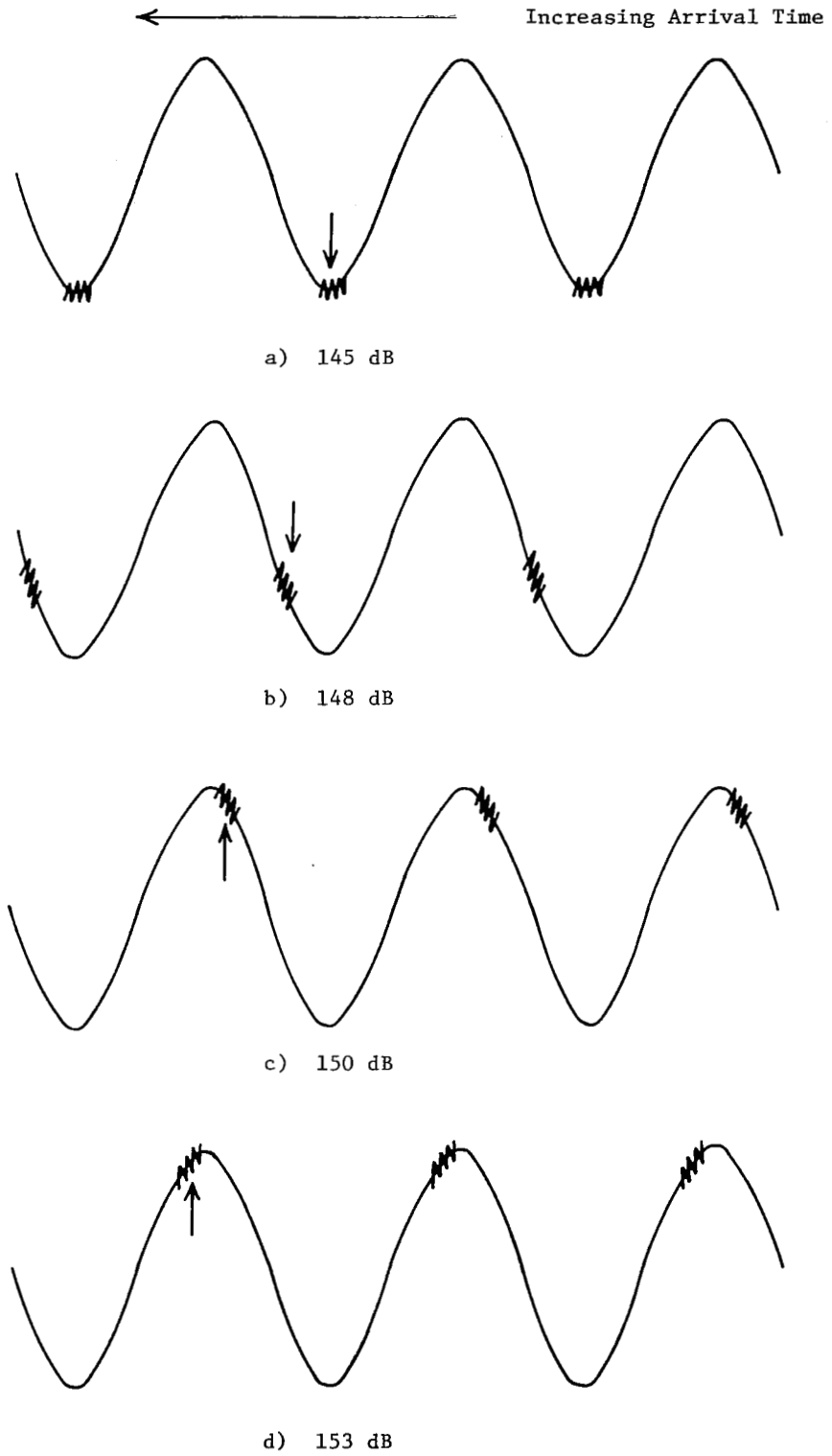


FIGURE B-4. TIME OF JET ARRIVAL AS INCIDENT LEVEL INCREASES